Czech Technical University in Prague
Faculty of Nuclear Sciences and Physical Engineering
Department of Physics

Study of cosmic ray generation in magnetized plasma jets in laboratory conditions

Master's thesis

Bc. Lenka Hronová

Supervisor: Ing. Michaela Kozlová, Ph.D.
Consultant: Ing. Miroslav Krůs, PhD.

Prague, 2022

Originální zadání DP

Prohlášení

Tímto prohlašuji, že jsem svou diplomovou práci vypracovala samostatně a použila pouze uvedené podklady.

Nemám závažný důvod nesouhlasit s použitím této školní práce ve smyslu §60 Zákona č. 121/2000 Sb., o právech souvisejících s právem autorským a o změně některých zákonů (autorský zákon).

V Praze, 2. 5. 2022 .....

Bc. Lenka Hronová

Acknowledgment:

The great gratitude goes to my supervisor Dr. Michaela Kozlová for her guidance, provided advices, many useful explanations and comments and also for her enourmous patience with my workflow. I would also like to thank to Dr. Miroslav Krůs for his many insightful comments. And of course my greatest gratitude goes to my family and the closest ones who have been here for me during the hard times of my studies.

Bc. Lenka Hronová

Název práce:

Studium generace kosmického záření v magnetizovaných plazmových výtryscích v laboratorních podmínkách

Autor: Bc. Lenka Hronová

Obor: Experimentální jaderná a částicová fyzika

Druh práce: Diplomová práce

Vedoucí práce: Ing. Michaela Kozlová, Ph.D.

Konzultant: Ing. Miroslav Krůs, PhD.

Abstrakt:

Škálování astrofyzikálních magnetizovaných dynamických procesů v laboratorních podmínkách je nyní možné díky rozvoji zařízení zvládajících kombinovat vysoce výkonné lasery produkující plazma a externí magnetická pole. Avšak vlastnosti plazmových výtrysků o nižší hustotě plazmatu, které vznikají na vzdálenější straně terče, dosud nebyly zkoumány v žádné obsáhlé studii. Vícesnímkové interferometry jsou unikátním nástrojem pro výzkum rychle se měnících podmínek v laserem generovaném plazmatu. Nový design čtyřsnímkového Mach-Zehnderova interferometru, mapujícího vývoj hustoty výtrysků plazmatu s více jak 20 variacemi terčových materiálů ve 4 různých časech, byl úspěšně navržen a implementován. S jednoduše nastavitelnými mezisvazkovými zpožděními, vysokou stabilitou a rychlou instalací je tento design ideální pro použití v budoucích experimentech zkoumajících plazmové výtrysky.

Klíčová slova: kosmické záření, vícesnímková interferometrie, laser, astrofyzikální jety, urychlování částic

Title:

Study of cosmic ray generation in magnetized plasma jets in laboratory conditions

Author: Bc. Lenka Hronová

Field of study: Experimental Nuclear and Particle Physics

Thesis type: Diploma Thesis

Supervisor: Ing. Michaela Kozlová, Ph.D.

Consultant: Ing. Miroslav Krůs, PhD.

Abstract:

Reproducing astrophysical magnetized dynamical processes in the laboratory is now possible due to the emergence of platforms able to couple high-power laser-produced plasmas and external magnetic fields. However, no comprehensive study of the properties of the low-density rear-driven plasma jets has been conducted to this extent. 'Multi-frame mode' interferometers provide a unique possibility in investigation of rapidly varying plasma's properties. A novel four-frame Mach–Zehnder interferometer was successfully developed and implemented for the first time, mapping the density evolution of the plasma jet with more than 20 varations of target material in four different times. With easily adjustable interbeam delays, high stability and fast installation, the interferometer design is ideal for the implementation in future plasma jet experiments.

Keywords: cosmic rays, multi-frame interferometry, laser, astrophysical jets, particle acceleration

Contents

List of Figures

Introduction

High-energy particles are formed not only on Earth, but also come to us from space and reach the highest energies ever observed [1]. What are the mechanisms that are able to accelerate those particles and what are the sources of these extremely high-energy cosmic rays?

Even though it is not possible to reach those energies in on-Earth experiments, we can study analogical processes in laboratory conditions and therefore shed light on those acceleration mechanisms that are responsible for the high-energy particles. Laboratory astrophysics is a field at the crossroads of plasma physics, particle physics and astrophysics, which transmits space events to our laboratories, thus helping us to better understand the dynamics of these processes. The aim of this thesis is the investigation of the properties of the low-density rear-driven plasma jets with various target materials. For this purpose, I have designed the novel four-frame Mach-Zender interferometer and successfully implemented it as a plasma diagnostic of (magnetized) jet density evolution. The study of magnetized jets in laboratory conditions is important for better understanding of reverse-shock dynamics, that can be responsible for accelerating particles to ultra-high energies [2].

The work is divided into four chapters. The first chapter summarizes the introduction to astrophysics, particle acceleration in space and physics of astrophysical jets. The latter part of this chapter is devoted to scaling the universe by using the intense laser systems in laboratory. The second chapter is dedicated to a short overview of plasma diagnostic stressing the basic principles of interferometry and shadowgraphy. The third chapter is devoted to a broader description of the interference principle and basic concepts of polarization, which are crucial for the development of a novel type of interferometer. The interferometer of Mach-Zehnder type is further described as suitable plasma diagnostics and overview of Fourier-transform method of fringe-pattern analysis is presented. In the fourth chapter, the modification of Mach-Zehnder interferometer to 'four-frame mode' is proposed and proof of concepts measurements are discussed. Finally, the preliminary results from the density evolution measurements of plasma jets in three different cases are presented: free jets, collisions with obstacle and magnetized jets.

Chapter 1

Basic concepts

Our universe has fascinated people since we first looked up. In ancient Greece, bodies in the sky were considered to be unchanging spheres moving uniformly in a circle and the celestial region was made of a different kind of matter from that on Earth. It was not until 17^{th} century that scientists began to maintain that the celestial and terrestrial bodies were made of similar kinds of material and were subject to the same natural laws. During the 19^{th} century most of the research was focused on the routine work of measuring the positions and computing the motions of astronomical objects [3]. Huge development of astrophysics is strongly related to the discovery of multitude of dark lines after decomposing the light from the Sun into the spectrum [4] in the second half of the 19^{th} century. Over the last decades we made enormous steps in exploring the universe: less than a century ago, people believed that the Milky Way was the only galaxy in the universe. Now we know there are 10^{11} galaxies within the observable universe, each containing some 10^{11} stars [5].

The first chapter is dedicated to the introduction to astrophysics, plasma physics and physics of cosmic radiation. Basic concepts of acceleration mechanisms in space and scaling of astrophysical phenomena are discussed further.

1.1 Introduction to astrophysics

Astrophysics is a branch of science that applies the laws of physics and chemistry to understand the universe. It explores topics such as the birth, life and death of stars, planets, galaxies, nebulae and other objects in the universe [3]. On the contrary, astronomy measures the positions, luminosities, motions and other characteristics of celestial subjects and cosmology covers the largest structures and the universe as a whole [6].

Astrophysics involves an interplay between theory and experiment, however the experimental part is somewhat different in the sence that astronomers cannot carry out controlled experiments. A huge part of studying the universe

is to perform observations of the various phenomena provided by nature [6]. The areas of modern astrophsics include the attempts to determine the properties of dark matter, dark energy and black holes, studies of Solar System formation and evolution, stellar dynamics and evolution, galaxy formation, magnetohydrodynamics, origin of cosmic rays, general and special relativity, and astroparticle physics [5].

Particle astrophysics studies elementary particle of astronomical origin and their relation to astrophysics and cosmology [3]. The field has begun in 1910, when a German physicist named T. Wulf measured the ionization in the air with the electroscope, an indicator of gamma radiation [7]. Soon after V. F. Hess hypothesized that some of the ionization was caused by radiation from the sky and his measurements have shown that 'a radiation of very high penetrating power enters our atmosphere from above' [8]. Cosmic Rays (CR) provided the only way in investigating new particles[1] until the advent of high-energy particle accelerators in the early 1950s. The majority of primary cosmic rays are protons (hydrogen nuclei), the rest is made up of alpha particles, neutrons or nuclei of heavier elements [9].

The energy spectrum of cosmic rays can be seen in Figure 1.1.

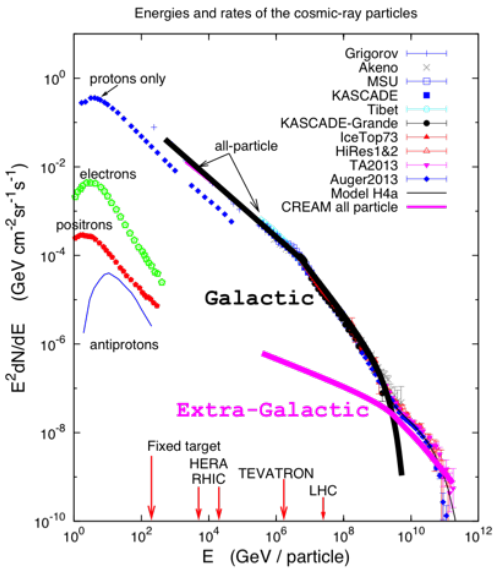

Figure 1.1: Spectrum of cosmic rays: The low region is dominated by cosmic rays from the Sun. Steeper part of the spectrum is dominated by rays produced in our Galaxy. At the highest energies a drastic suppression is expected from the interaction with the cosmic microwave background [5].

[1] In 1932 the positron was discovered - the first particle of antimatter, that was followed by the muon in 1937, the pion, the kaon and several more [9].

The low energy region is dominated by cosmic rays from the Sun (solar wind), further the spectrum becomes steeper for energy values less than ∼1000 TeV. This region is dominated by cosmic rays prudced by sources in our Galaxy. For even higher energies the spectrum is even more steep and the change of slope occurs at the point called "the knee" [5]. It is believed that cosmic rays of these energies are produced by extragalactic sources, mostly supermassive black holes at the centre of other galaxies [10]. The other change of slope "the ankle" [11] occurs at even higher energies, as at the highest energies a drastic suppression is expected from the interaction of long-traveling particles with the Cosmic Microwave Background (CMB)[2]. Cosmic rays above this limit are know as the extreme-energy cosmic rays [13] and they are supposed to be from within 50 kpc or are more massive particles such as alpha particles and nowadays there is no consensus regarding the mechanism of their creation[3] [12].

High-energy particles from the Sun or outer space can be detected directly by satellites in space. Cosmic rays with energies exceeding 10^{13} eV can be detected indirectly via observation of the cascading shower they produce in the atmosphere [6]. Observation and analysis of properties of high-energy particles in high-energy astrophysics sources play an essential role in exploring the underlying physical processes.

Curent challenges include characterization of dark matter and dark energy or why is there so much more matter than antimatter [6, 5]. Other unsolved task that is relevant to the topic of this thesis is to found the principles and sources of particle acceleration to energies that are incomparably larger than of those produced on Earth. For example, the cosmic ray spectrum contains partciles with energies as high as 10^{20} eV, where proton-proton collision at the Large Hadron Collider occurs at an energy of 10^{12} eV. These high-energy beams of extraterrestrial origin are coming from regions where highly energetic phenomena take place that we cannot directly explore and they may advance our knowledge of fundamental physics and interactions as well as the highest energy events occuring in the universe [5].

[2]The GZK limit (Greisen-Zatsepin-Kuzmin) is a theoretical limit calculated independantly by each of its three developers on the kinetic energy of CR protons based upon the expected interaction of the protons with CMB photons, if they travel through the CMB distances on the order of 50 kpc and above [12].

[3]The particle with the highest energy ever measured was detected on 15th October 1991 and had an energy of 320 EeV [14].

1.2 Particle acceleration mechanisms in space

About once per minute, a subatomic particle enters the Earth's atmosphere with an energy larger than 10 J. Somewhere in the universe there are acceleration mechanisms that can accelerate single protons to 10× larger energies than we are able on Earth. But how?

Particle acceleration mechanisms have different assumptions and may be used in different astrophysical contexts. Usually, those mechanisms are associated with the interfaces between domains of plasma - regions where a plasma dominated by one configuration of charges and magnetic fields, collides with a different configuration of charges and magnetic fields. Those collisions can generate changes in the field configurations which can accelerate charged particles [15].

1.2.1 Direct acceleration by electric field

Electric fields are in space in macroscopic scale shielded by the presence of conductive plasma that means that the direct acceleration by electric field is not possible while $\langle \mathbf{E} \rangle = 0$. The Debye length defined by Equation (1.1) is giving us the distance in that the electric field is effectively shielded [16]:

$$\lambda_D = \sqrt{\frac{\varepsilon_0 kT}{n_e q_e^2}}, \tag{1.1}$$

where k is Boltzmann's constant , T is temperature, n_e is density, q is charge, ε is vacuum permitivity. This distance is shorter with the higher density of charge carriers[4] [17]. The exceptions for this case are magnetospheres of rotating black holes or neutron stars, where localized electric field can exist due to magnetic reconnections [18].

1.2.2 Stochastic acceleration

In this type of acceleration mechanism the particles are accelerated in a large number of repetitions [6]. Fermi second order acceleration [19] is one of examples of stochastic acceleration mechanisms. The particles are accelerated in magnetised gas clouds and can either gain but also lose energy as it is illustrated in Figure 1.2.

[4] For example it is 10 meters for interstellar space and 100 km for intergalactic space [17].

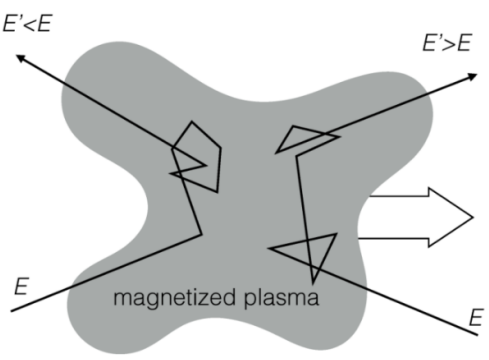

Figure 1.2: The particle enters the gas cloud with the energy E and interacts by elastic scatterings with other particles of the cloud. They can either lose ($E^{'} < E$) or gain ($E^{'} > E$) energy [17].

The cross section of the collisions can be expressed by following relation [17]:

$$\frac{\mathrm{d}n}{\mathrm{d}\Omega} \propto (1 - \beta \cos\theta_1), \tag{1.2}$$

where β is a gas cloud velocity and θ_1 is the angle between the vector of the gas cloud velocity and the velocity of the particle flying out of the cloud.

The mean energy gain of the particle is [17]:

$$\left\langle \frac{\Delta E}{E} \right\rangle = \frac{4}{3}\beta^2. \tag{1.3}$$

That is why this mechanism is called Fermi 2^{nd} order acceleration because of the energy gain dependance on the power of β squared. Typical values for the velocity of the gas cloud in space are $\beta \ll 1$ so the effectivity of this process is quite low and it is necessary to have a huge number of collision to achieve the highest energies [20]. The slow energy gain is also being limited by energy loss of cosmic radiation [21, 19].

1.2.3 Shock acceleration

A shock wave can be generally defined as a transition layer which propagates through a plasma and changes its state [22]. The wave compresses the plasma and some of the kinetic energy of the incoming plasma is transferred to internal degrees of freedom of the downstream plasma (plasma before the shock wave). The thickness of the shock front (the transition layer) is determined by the physical process responsible for this energy conversion [23]. This type of acceleration is a fundamental particle acceleration process in both space

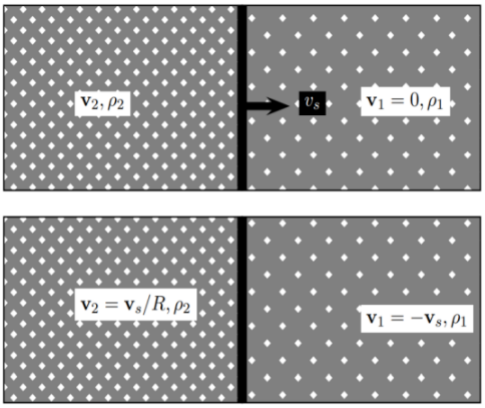

Figure 1.3: Schema of variables in the areas before and after the shock, where ν_1 and ν_2 are the fluid velocities, ϱ_1 and ϱ_2 are the fluid densities and R is the compression ratio [17].

physics and astrophysics as a mechanism for generating highly energetic particles in a variety of sources as supernovae [24], the interstellar medium [25] or the Earth's bow shock [26, 27].

During the Diffusive Shock Acceleration (DSA), also known as Fermi first order acceleration) in the presence of strong shock waves around supernovae explosions are particles diffusively scattered by magnetic fluctuations in both areas before and behind the shock and repeatedly accelerated in multiple crossings [28]. The DSA is a system with multiple shocks and is not well understood yet [22].

The conditions before and after the shock wave as we can see in Figure 1.3 can be expressed by Rankine-Hugoniot equations [29] for conservation of mass, momentum and energy. Through solution of these equations we can derive the velocity of material compression by shock wave and find the ratios between densities and velocities in the regions before and after the shock [17].

The equation for energy gain of the particle is [17]:

$$\left\langle \frac{\Delta E}{E} \right\rangle = \frac{4(\nu_2 - \nu_1)}{3}, \tag{1.4}$$

where ν_1 and ν_2 are the fluid velocities after and before the wave. The maximal energy of the particles E_{max} depends on many factors but the estimation for nonrelativistic shock waves is [24]:

$$E_{max} = 5 \times 10^6 Z \left(\frac{B}{10^{-5}\mathrm{G}} \right) \mathrm{GeV}, \tag{1.5}$$

where Z is the particle charge and B is the strength of the magnetic field. In a more general case with an oblique shock, the particles drift along the shock

front due to the change in magnetic field and get accelerated by the electric field parallel to the drift motion. This process is called Shock Drift Acceleration (SDA) and is believed to be important for acceleration at bow shocks and interplanetary shock [28].

The radiative characteristics of high-energy astrophysical sources depend on properties of high-energy particles they produced [5]. The conditions for source of the high energy cosmic rays are:

- Geometry: Particles that are being accelerated should be maintained within the object during the acceleration.
- Power: We need necessary energy for the acceleration process.
- Radiation losses: During the acceleration the particle should gain more energy than its radiation loss.
- Interaction losses: During the acceleration the particle should gain more energy than its losing due to its interaction.
- Emissivity: The density and power of sources must be enough to account for the observed flux.
- Coexisting radiation: The accompanying photon and neutrino flux, and theenergy CR flux, should not be greater than the observed fluxes [9].

From the main idea behind the concept of Fermi's first-order acceleration it becomes clear that when Larmour radius r_L approaches accelerator's size it is difficult to magnetically confine the cosmic rays to the acceleration region and further process up the energy of the particles [30]. In addition, if we take into account the effect of the characteristic velocity βc of the magnetic scattering centers, we get the general condition for the maximum energy acquired by particle travelling in a medium with the magnetic field B [31]:

$$E_{max} \sim 2\beta c Z e B r_L. \tag{1.6}$$

It is known as Hillas criterion and it can be depicted in the Hillas plot in Figure 1.4. This condition shows that very few objects can generate particles of the highest energies: either they are highly condensed with strong magnetic fields or enermously extended [5].

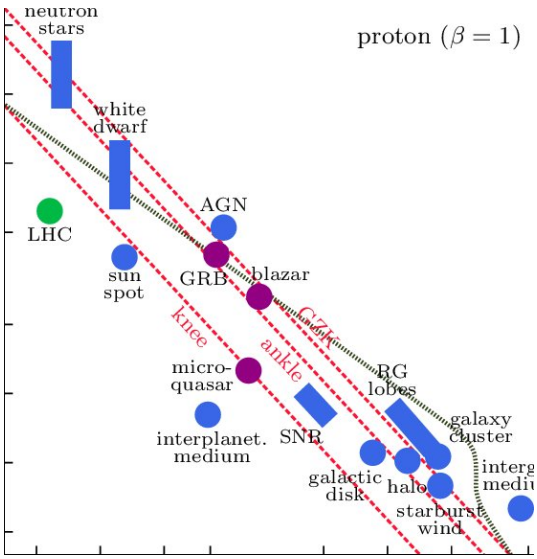

Figure 1.4: Hilas plot is showing upper limit on the reachable CR energy dependent on the size of the acceleration region and magnetic field strength [31].

1.2.4 Pulsars

Pulsars are neutron stars with a strong magnetic field (10^8 T) that radiates electromagnetic radiation in the direction from magnetic poles. They are the remenants after supernovae explosion, have very short period of rotation (ms - s), radius smaller than 20 km and density is similar to a density of atomic nucleus ($\approx$ 10^{17} kg/m^3) [32]. The axes of rotation are different from axes of agnetic field, which is rotating very fast and generates electric field that can accelerate particles [33, 34].

1.2.5 Binary systems

The binary systems are two stars orbiting a common center of mass [27]. If we consider the pair to be a combination of pulsar or neutron star with the classical star, the material from the classical star can be pulled down to pulsar/neutron star. As a consequence the moving plasma is creating strong magnetic fields in the surrounding of the neutron star, where the particles can be accelerated to high energies [27].

1.2.6 Active Galactic Nuclei

The Active Galactic Nuclei (AGN) are with their large accreation discs the brightest sources of radiation in space [17]. They are acompanied by ultra-relativistic jets that are good candidates for sources of the radiation of the highest energies [5]. In jets the particles can be accelerated by shock waves, however

to see the particles from these sources they need to be in a proper position [17]. In 2007 the article [35] that presented good correlation between the direction of incoming ultra high-energy cosmic radiation and AGNs was published, but after obtaining higher statistics the correlation decreased [17] and more data are needed to determine the accuracy.

1.2.7 Z-burst

Z-burst is one of the proposed models to expain the emergence of the cosmic radiation of the higest energies [36]. This model is taking into account the anihilation of (resonant) neutrinos and (relikt) antineutrinos pair to Z boson that almost immediately decays into hadrons and leptons [17]:

$$\nu_j + \bar{\nu_j} \rightarrow Z. \tag{1.7}$$

The cross section of this process is $\sigma = 4.2 \times 10^{-32}$ cm^{-2} and the resonant energy is:

$$E^R_{\nu_j} = 4(\mathrm{eV}/m_{\nu_j}) \times 10^{21}\mathrm{eV} \tag{1.8}$$

where m_{ν_j} is mass of the neutrino. The Z boson has the 70% propability to decay into hardons. Aproximetally one pair of baryon-antibaryon (p or n), 17 charged pions and 10 neutral pions are created [37] as the end product of the decay and are reffered as Z-burst. The nucleons are candidates for the primary particles with energy above the GZK-cutoff [17].

1.3 Plasma in space

Almost all astrophysical objects are in the state of plasma. The general description of this state of matter was given in the previous research project [38], where we define it as a partially or completely ionized mixture of positive ions and electrons and describe it by characteristics such as Debye length (Equation 1.1), plasma parameter [16]:

$$N_D = \frac{4}{3} n_e \pi \lambda_D^3 \tag{1.9}$$

and plasma frequency, which is defined as [16]:

$$\omega_p^2 = \frac{n_e e^2}{\varepsilon_0 m_e}, \tag{1.10}$$

where m_e is the electron mass and ε_0 is the vacuum permittivity. Shortly we can define plasma as an ionized gas in which collective effects dominate over collisions [39]:

$$\lambda_D \ll \text{size and } N_D \gg 1. \tag{1.11}$$

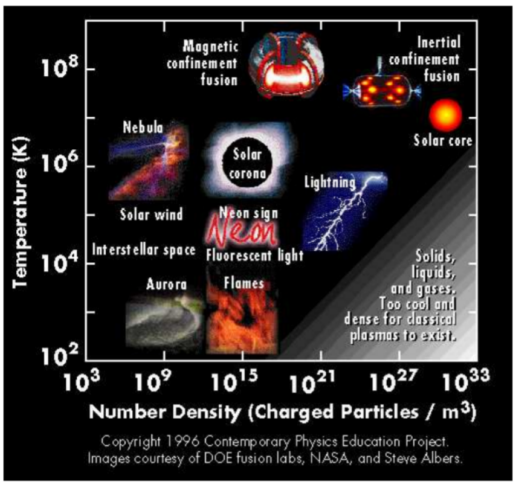

Figure 1.5: Various types of plasma according to its density and temperature [40].

There are many variations of natural and man-made plasmas of wide range of density and temperatures as we can see in Figure 1.5. Understanding the basic properties of plasmas is important for understanding many other and more difficult processes in solar physics, space physics, astrophysics and for the developement of controlled thermonuclear fusion [39].

Plasma reacts very strongy to electromagnetic forces [40]. Space plasmas moving though a magnetic field generating its own electric current, can act as an unipolar inductor, and thus conduct electricity better than metals. Magnetic fields from electromagnetic currents are then able to make plasma pinches. They also constrict particle beams seen in astrophysical jets [41].

1.3.1 Astrophysical jets

Highly-collimated, supersonic jets (see in Figure 1.6) are outflows of ionized matter emitted as an extended beam along the axis of rotation [41] and are found in many diverse objects in the universe. Examples range from large scale jets emarging from galaxies [42] to those ejected form stars in their formation stage known as Young Stellar Objects (YSO) [43] as we can see in Table 1.1 [41, 44].

The topic of a common lauching mechanism is still of active interest while jets share many similar features [46]. They reach lengths of around 0.1 pc and are highly collimated over long distances (length to width ratio is 10 or more), which is caused by the presence of the surrounding interstellar medium, external magnetic fields and radiation cooling [47]. However, the importance of these individual components is still not fully understood, especially at greater distances from the star, where the magnetic field is significantly

Object	Type	Physical system
Young Stellar objects	stellar	Accreting young star
Massive X-ray binaries	stellar	Accreating neutron star or black hole
Black hole X-ray transients	stelar	Accreating black hole
Low mass X-ray binaries	stellar	Accreating neutron star
Symbiotic stars	stellar	Accreating white dwarf
Planetary nebulae nuclei	stellar	Accreating nucleus (or "interacting winds")
Supersoft X-ray sources	stellar	Accreating white dwarf
Active galactic nuclei	extragalactic	Accreating supermassive black hole

Table 1.1: Overview of jet sources and its type.

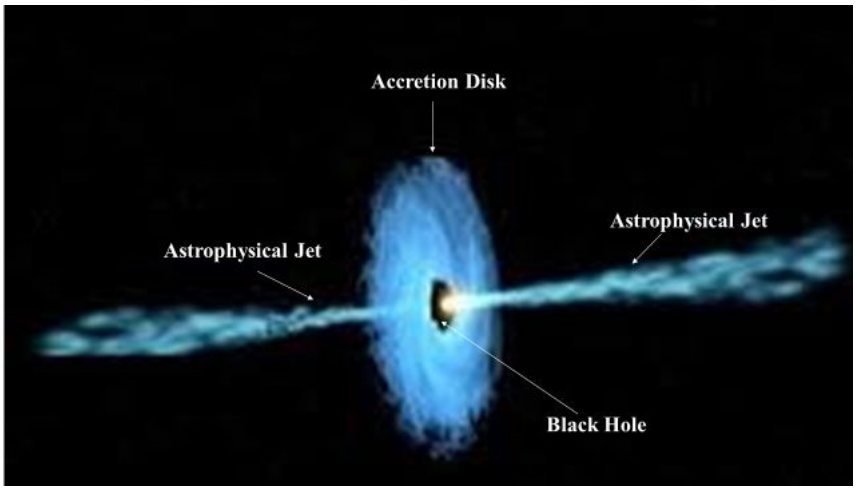

Figure 1.6: Astrophysical jet and accreation disk around black hole [45].

weakened. Jets propagating at speeds of 100-400 km/s from their sources were observed [48]. The structure of the jets has been investigated in a number of experiments and by many simulations and is best described as a structure consisting of a dense central region and a less dense 'cocoon' [47].

Astrophysical jets are ideal candidates as sources of radiation of EeV energies [49, 25]. They are often supersonic, transport strong magnetic fields and produce strong shock waves, so turbulence are important in their presence [41]. All of those are proper conditions for particle acceleration by scatterings in a turbulent velocity fields or across a shock [50], shear layer [51] or reconnection site [52]. The energy increase of the particle is given by moving charged particle through a $-\mathbf{v} \times \mathbf{B}$ electric field [41]. As imaging of jetted sources is providing us important clues about particle acceleration, we can say that in some jet sources there are particles being accelerated at the surface of a strong shock. The most universal observational signature of astrophysical jets is synchrotron radiation produced by relativistic electrons spiralling in magnetic fields. In generall, power-law spectra are common in jetted systems [53].

1.4 Scaling

The dynamics in the universe is characterised by high energies (high-energy cosmic rays, gamma rays, neutrinos), temperatures and densities (supernovae explosions, gamma bursts) and strong fields (near the black holes and neutron stars) [1]. To look closer and try to examine those events and dynamical processes was for a long time challenging and apart from direct observation or sending satelites it was necessary to find an alternative way to study the universe [54]. The existence of sufficiently intense laser beams[5] (Figure 1.7) and the development of new diagnostic methods and laboratory experiments have become this alternative [54].

Laboratory astrophysics is a branch of physics which attempts to simulate celestial bodies in a terrestrial laboratory. It was pioneered by Kristian Birkeland [40] and it interweaves knowledge from astrophysics, particle physics and plasma physics, to investigate various phenomena, for example by carefully scaling dimensionless parameters [54]. The idea of laboratory simulation is based on the fact that both systems - astronomical phenomena and laboratory enviroments, are described by pure hydrodynamic or magnetohydrodynamic motions, thus there exists similarities [25] as we will talk about in the last section of Chapter 1. To study the universe in laboratory a number of tools

[5] In 1985, Dona Strickland proposed the use of chirped pulse amplification to successfully amplify the laser beam at a higher intensity than hitherto possible [55].

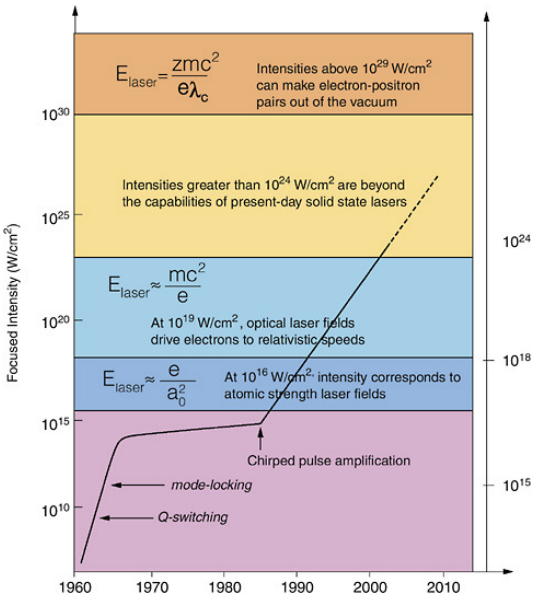

Figure 1.7: Development of laser intensity. The main progress was done by D. Strickland when she proposed the Chirped Pulsed Aplification method for lasers in 1985 [55].

are used such as terrellas, pinches, dense plasma focus, electrical discharges and lasers [40].

1.4.1 Laser application in studying the universe

The possibility of creating space conditions on a small scale in a laboratory environment allows us multi-point measurements, their repeatability, controllable conditions and, among other things, reduced costs [54]. Generally lasers can help in three different areas:

1. Calibration: Astrophysics measurements rely on photon measurements from the following processes: atomic and molecular spectra, synchrotron radiation, Compton scattering, etc. Accurate calibration in laboratories helps to verify these measurements [56].

2. Dynamic processes: Accurate simulation of space conditions in the laboratory is not possible. However, most magneto-hydrodynamic processes are scalable. Examples are astrophysical jets, turbulence, shock waves and instabilities [57].

3. Basic cosmological questions: Study of Hawking radiation, study of quantum gravity [54].

The laboratory measurement itself can be divided into two types according to whether we want to mimic the overall geometry of the system or study the local properties of the process [58]. Such measurements were suggested already shortly after the discovery of laser. However it took a decade to develop powerful lasers capable of delivering the intensity of $10^{13} - 10^{16}$ W/cm^2 onto the target that is needed to generate the required laser plasma cloud of sufficient high kinetic energies [59].

1.4.2 Laser generated plasmas

One way to ionize a neutral gas is to use a laser pulse that can be focused on a small area to achieve high energy flux densities. The moment the laser hits a solid target, it heats it up [60]. It should be noted that laser radiation is absorbed only at lower plasma densities than the critical density n_c given by [61]

$$n_c = \frac{\omega^2 \varepsilon_0 m_e}{e^2}, \tag{1.12}$$

where ω is frequency of laser radiation [62]. If this condition is met, the laser light is absorbed by the mechanism of inverse bremsstrahlung (attenuation of light waves due to electron-ion collisions). The absorption coefficient κ is defined as [60]:

$$\kappa = \frac{1}{2c\tau_{ei}\left(\frac{\omega_p^2}{\omega^2}\right)\left(1-\frac{\omega_p^2}{\omega^2}\right)^{-1/2}}, \tag{1.13}$$

where τ_{ei} is the collision time between electrons and ions. This relationship suggests that higher density plasma absorbs the laser beam better. Current laser with intensities of $10^{13} - 10^{21}$ W/cm ^{2} are able to ionize the gas and create a plasma in a single pulse [63]. The study of laser plasma today helps with the research of thermonuclear fusion, the acceleration of particles with field gradients of orders greater than those achieved in conventional accelerators, or the study of the dynamics of space processes [62, 54]. Laser generated plasma is characterized by very short temporal existence and fast evolving parameters [63]. This needs to be considered while choosing suitable plasma diagnostics.

1.4.3 Astrophysical jets in laboratory conditions

Due to the development of High-Energy Density facilities, which allow reaching the extreme physical conditions in terms of pressure, density and temperature we are able to create astrophysical jets in laboratory conditions [64].

Plasma jets are created in experiments, when sufficiently intense laser irradiates a solid target (materials such as copper, aluminium, iron or titan can be used.). These jets have dimensions in the order of millimeters, but reach similar velocities of around hundreds of km/s [65].

The most important scaling parameters are:

- Mach number M: relates the jet velocity to velocity of the sound. In plasma physics the Alfven velocity v_A:

$$v_A = \frac{B}{\sqrt{\mu_0 n}}, \tag{1.14}$$

  is used. The Mach number is then define as:

$$M = \frac{v}{v_A}, \tag{1.15}$$

  where v is the jet velocity.

- Cooling factor χ: relative importance of different cooling processes.
- Density ratio η: jet density to ambient density.

In Table 1.2 we can see typical values for astrophysical jets and values that were achieved in the study of jet formation and propagation in the laboratory [47].

1.4.4 Density of the jets

To get the density of plasma in space we use its connection to index of refraction [67]. Index of refraction n characterise the change of propagation velocity v of the electromagnetic radiation in two different enviroments [68]:

$$n = \frac{c}{v}, \tag{1.16}$$

where c is the speed of light. For the wavelength in the enviroments with n we have the relation $\lambda = \frac{\lambda_0}{n}$ [68], where λ_0 is the wavelength of the same radiation in the vacuum. The optical path is defined as a curve integral of the first kind [61]. By integrating over this curve[6] we can calculate the resulting path

[6] According to Fermat's principle the light propagates along the curve C that corresponds to the shortest propagation time [68].

Scaling parameters		
Name	Astrophysical jets	Laboratory jets
Mach number	10,0 - 25,0	9,0 - 12,0
Cooling factor	0,1 - 10,0	80,0
Density ratio	1,0 - 10,0	3,5
Other characteristic parameters		
Length [cm]	$3,0.10^{17}$	0,5
Radius [cm]	$7,5.10^{15}$	$15,0.10^{-3}$
Density of particles [cm^{-3}]	20,0	$1,5.10^{18}$
Temperature [eV]	1,0	100,0

Table 1.2: Comparison of scaling [47] and other [66] parameters of astrophysical and laboratory jets.

difference as we can assume that optical inhomogeneities cause infinitesimally small shifts of the beam.

Generally for two beams with two different optical paths we can write:

$$\delta = l_1 - l_2 = \int_{C_1} n \, \mathrm{d}s - \int_{C_2} n \, \mathrm{d}s = \lambda_0 \cdot \left(\int_{C_1} \frac{1}{\lambda} \, \mathrm{d}s - \int_{C_2} \frac{1}{\lambda} \, \mathrm{d}s \right), \tag{1.17}$$

where $n(x, y, z)$ is the index of refraction in the point (x, y, z) and $\mathrm{d}s$ is the element of the curves C_1 and C_2. If we choose the coordinate system so the beam is going along the z axes we can define the path difference by [69]:

$$\delta = \int_a^b [n(x, y, z) - n_0] \, \mathrm{d}z, \tag{1.18}$$

where n_0 is the index of refraction in the environment without plasma, a and b are the coordinates of the beginning and the end of plasma along the curve parallel to z axes.

Another step to complete the analysis is the Abel transformation in which we use the mirror symmetry of the plasma jet because we have a symmetrical Gaussian laser beam that is irradiating the target. From the measurement of n in one direction, we are able to get the radial distribution in the given enviroment [61]. Using Abel transformation to Equation (1.18) we get:

$$\delta(x, y) = \int_0^{z_0} 2[n(x, y, z) - n_0] \, \mathrm{d}z = 2 \int_y^R \frac{[n(r, x) - n_0] r \, \mathrm{d}r}{\sqrt{r^2 - y^2}}, \tag{1.19}$$

where r and R are coordinates in radial system according to Figure 1.8. Using inverse Abel transformation we can express the space distribution of index

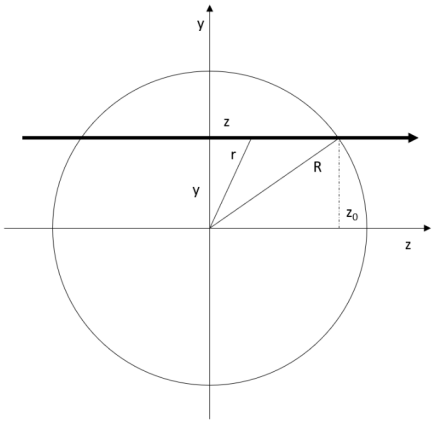

Figure 1.8: Schema of coordinates in cylindrical symmetric environment.

of refraction [61]:

$$n(r,x) = n_0 - \frac{1}{\pi}\int_r^R \frac{\partial\delta(x,y)}{\partial y}\frac{\mathrm{d}y}{\sqrt{y^2-r^2}}. \tag{1.20}$$

The path difference δ is related to the phase difference Φ of the wave that goes through given enviroment by [61]:

$$\Phi(x,y) = \frac{2\pi}{\lambda_0}\delta(x,y) + \varphi_0, \tag{1.21}$$

where φ_0 is a constant equal to a phase difference of both waves as a consequence of path length differences of each of them. The final relation for the index of refraction is [70]:

$$n(r,x) = n_0 - \frac{\lambda_0}{2\pi^2}\int_r^R \frac{\partial\Phi(x,y)}{\partial y}\frac{\mathrm{d}y}{\sqrt{y^2-r^2}}. \tag{1.22}$$

To link the index of refraction with the electron density we write first the dispersion relation [16]:

$$\omega^2 = \omega_p^2 + c^2k^2. \tag{1.23}$$

Using Equation (1.16) and substituting ω_p with Equation (1.10) we can get the index of refraction from Equation (1.23):

$$n^2 = 1 - \frac{N_e e^2}{m_e\varepsilon_0\omega^2} \tag{1.24}$$

and if $\omega \gg \omega_p$ we can use:

$$n \approx 1 - \frac{N_e e^2}{m_e \varepsilon_0 \omega^2}. \tag{1.25}$$

Finally, the electron density can be expressed as [16]:

$$N_e = \frac{4\pi^2 m_e \varepsilon_0 c^2}{e^2 \lambda_0^2}(1 - n^2). \tag{1.26}$$

We can see that the index of refraction of the plasma enviroment is smaller than one and phase velocity of the wave is higher than then the speed of light. That is possible because the phase velocity does not have the meaning of carrying the information [16].

1.4.5 Magnetized jets

It is commonly accepted that magnetic fields play a crucial role in the process of jet formation in e.g. galactic jets (Poynting-flux dominated) and YSO jets (kinetic dominated) [64]. Due to the emergence of platforms able to couple high-power laser-produced plasmas and external magnetic fields in a laser enviroment, it is possible to study magnetized dynamical processes in the laboratory and to collimate the plasma flow as it can be seen in Figure 1.9 without using a tube [71]. Recent radiations of hydrodynamic simulations show the importance of the coupling between magnetic fields, radiation process and extreme hydrodynamics, which can give rise to a wide variety of dynamical behaviors depending on which regime we are located [71]. With astrophysical jets, huge magnetic fields ($>$ 1000 T) are associated. This fact leads to extremally high fields (the order of 10^5 T) that are unrealistic to achieve in laboratory conditions [72]. In the polar regime (for magnetic fields below 3000 T) the magnetic field has only one effect: the collimation of the accreated plasma flow. The parameters important to evaluate are two [71]:

- β_{ram} parameter which evaluates the ration between the ram pressure $\varrho\nu^2$ and the magnetic pressure $B/2\mu_0$,
- Reynolds number R_m which gives an indication on the diffusivity of the magnetic field inside the plasma and is define as

  $$R_m = \mu_0 \sigma u L, \tag{1.27}$$

  where u is the flow velocity, L is the characteristic length and σ is the electrical conductivity.

Also, the radiation plays an important role and the laser produced plasma should have a magnetic pressure dominant over ram pressure [71].

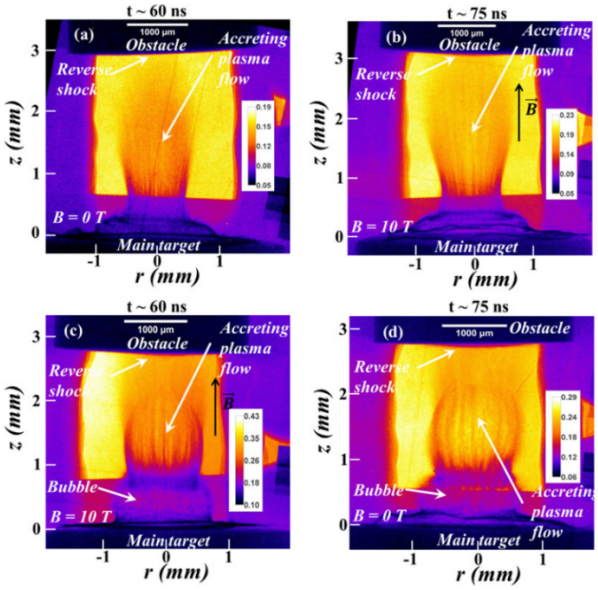

Figure 1.9: Difference between laboratory jets without (a),(b) and with (c),(d) the presence of the magnetic field in two different times. The images are taken by X-ray radiography [71].

1.4.6 Why is scaling possible

Possibilities of laboratory simulations of various phenomena in space were analysed on the bases of similarity criteria, properties of collisionless interactions and parameters of laser-produced plasmas [73]. Experiments can be relevant to astrophysical jets due to the invariance of the ideal fluid equations describing both systems. A correct scaling of an astrophysical jet is possible if several dimensionless parameters describing both systems are in correct regime [58]. So although the powerful facilities we now have provide us a great opportunity in studying the extreme phenomena at the laboratory scales, it is challenging to create and maintain a laboratory system which is similar to its astrophysical counterpart. This actually leads us to a fundamental question of laboratory astrophysics which is the determination of relevance of these experiments [74]. Ideally, there should be a match between the parameters of the modeled phenomenon and the experiment. However, these requirements are difficult to meet and during the experiments there are only a few basic parameters of the same value [58]. Overall, the scaling laws play a crucial role in all high-energy density physics, since they can be used to adapt a target design from one powerful facility to another and can be a powerful tool for numerical simulations [74].

Chapter 2

Plasma diagnostic

In this chapter we will discuss laser plasma diagnostics. Further we present two types of non-destructive optical plasma diagnostic (interferometry and shadowgraphy) in more detail.

2.1 Overview

Plasma diagnostics are set of instruments, methods and techniques to measure plasma properties [75]. The complete statistical describtion is possible to get by the knowledge of distribution function for all appropriate positions $\mathbf{x}$ and velocities $\mathbf{v}$ in given time t together with the electromagnetic fields averaged over all possible realizations of the particle distributions [76]. However that is generally task beyond our practical capabilities and it is sufficient to determine only the low order moments of this function.

The particle density n is define as:

$$M^0 = \int f(\mathbf{v}) \mathrm{d}^3\mathbf{v} \equiv n, \tag{2.1}$$

where M^0 is the scalar moment of the distribution function. The particle velocity $\mathbf{V}$ is a vector moment:

$$\frac{1}{n}\mathbf{M}^1 = \int f(\mathbf{v})\mathbf{v}\mathrm{d}^3\mathbf{v} = \mathbf{V}. \tag{2.2}$$

Analogically we can define temperature T and heat flux tensor Q as the second and the third order moment of the distribution function [76].

Generally, we can divide the methods into destructive and non-destructive diagnostics which differs by the amount of the influence they have on plasma properties.

Further, we can divide plasma diagnostics into [77]:

- Electrostatic probes: A probe is inserted into the plasma, to which voltage is applied to determine the volt-ampere characteristic. An electron temperature can be obtained from this. There are several types of probes. Each is suitable for measuring different properties in different types of plasma [78].

- High frequency (microwave) methods: The plasma is exposed to microwave radiation and a change in the propagation constant is observed after passing through the plasma waves. Concentration data can thus be obtained. Due to the random movement of electrons, as a consequence of their acceleration in the field of atoms, a noise current is created. By those methods, the electron temperature can be obtained [79].

- Optical methods: They can be based either on plasma irradiation or on analysis and evaluation of the radiation spectrum of the plasma itself. This group includes diagnostics such as optical emission spectroscopy and interferometry [80].

- Corpuscular diagnostics (mass spectroscopy): It is used to study the chemical composition of plasma [81].

The key parameters for the description of laser plasma are density and temperature. Under normal conditions, the degree of ionization is not negligible and it is necessary to recognize between the density and ionization of electrons, positive and neutral atoms. However, in the initial times of the plasma's existence, both the temperature and the density of the plasma are given mainly by the contribution from the temperature and the electron density. The plasma temperature can be determined during the entire expansion process by means of visible spectroscopy. However, there are several options for obtaining plasma density, such as plasma spectroscopy, microwave and laser interferometry, or Thomson scattering. Each of these methods is more suitable for certain types of plasma [63, 38].

2.2 Interferometry

The wave nature of light was first illustrated through experiments on diffraction and interference [48]. Nowadays, interferometric techniques are one of many non-destructive mothods used for measurements of a wide range of physical variables including refraction index, deformations, temperature gradients, etc [61]. During those measurements one or several interferometric fringe patterns that contain the information of the physical variable are generated by merging two or more sources of light and needs to be interpreted

in order to recover the parameters [61]. Interferometers have various designs as they are used for measurements of objects of various sizes and very often they are used to make measurements of very small variations such as 10^{-19} m that are not achievable by any other method [82, 83]. On the other hand we can use them to measure enormous expanses of gas in the universe [84].

Laser interferometry is allowing us precise measurements in the early stage of plasma expansion. In those moments the continuum associated with bremsstrahlung and recombination emission does not allow clear detection of emission lines [63]. In general, the laser is divided into a reference and an object beam, where the object beam passes through the object with different optical density (plasma). After recombination with a reference beam, an interference pattern is created from which a free electron density can be obtained that is directly proportional to the refractive index [85]. The variance in the refractive index is the same as the change in the path length of the beam passing through the plasma. The phase shift is obtained from the amplitude of the interference fringes after recombination of both beams. The time resolution of the interference depends on the pulse length of the diagnostic beam and the timing of the detection device. If the plasma evolution is equal to or shorter than the laser pulse length, then the interference fringes blur. The laser wavelength should be far from the resonant absorption value of the plasma so that the contributions to the refractive index from bound electrons are negligible compared to free electrons [86].

2.3 Shadowgraphy

Another type of optical non-destructive plasma diagnostic is shadowgraphy. Its advantage is very simple experimental layout that enables to get images of the plasma for qualitative evaluations on its shape and profile [87]. The laser light traverses the plasma, where it is refracted and creates an intensity image, so no reference beam is used [76]. The variations in intensity occurs, because the laser is deviated by a given angle, which varies across plasma as we can see in Figure 2.1 [76]. The examples of shadowgraphy imagining of plasma jets without and with external magnetic field are shown in Figure 2.2.

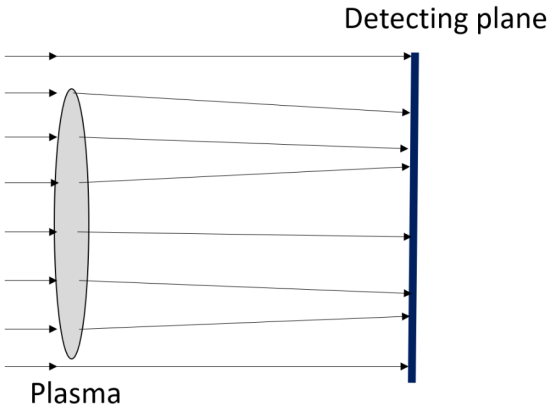

Figure 2.1: Basic concept of shadowgraphy. The direction of the incoming straight beam is altered by different plasma density.

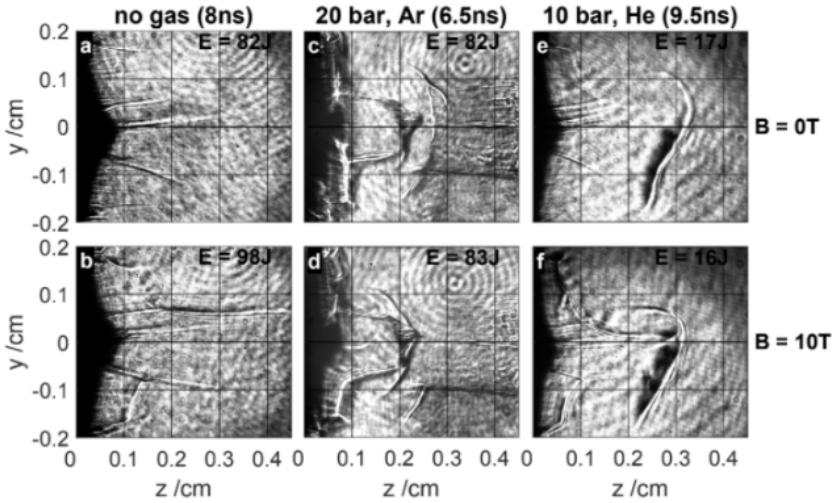

Figure 2.2: Shadowgraphy imaging showing jets and shocks without magnetic field (top row) and with a 10 T magnetic field directed out-of-plane (bottom row). The energy of the laser beam was around 20 J [88].

Chapter 3

Interferometry

We have introduced laser interferometry as one of the possible plasma diagnostic. In this chapter we will focus on the theoretical description of polarization and wave interference as we use both of these concepts in the modified design of Mach-Zehnder interferometer discussed in the second part of this chapter and in Chapter 4. The last section is dedicated to the mathematical background of fringe pattern analysis.

3.1 Electromagnetic radiation and plane wave solution

Light is electromagnetic radiation so it satisfies Maxwell equations [69]:

$$\nabla \times \mathbf{E} + \frac{\partial \mathbf{B}}{\partial t} = 0 \qquad \nabla \cdot \mathbf{E} = \frac{\varrho}{\varepsilon} \tag{3.1}$$

$$\nabla \times \mathbf{B} - \varepsilon\mu\frac{\partial \mathbf{E}}{\partial t} = \mu\mathbf{j} \qquad \nabla \cdot \mathbf{B} = 0, \tag{3.2}$$

where $\mathbf{E}$ is electric intensity, $\mathbf{B}$ is vector of magnetic field, ϱ is a charge density, ε is dielectric permittivity, μ is magnetic permeability and $\mathbf{j}$ is flux density. These equations relate the interplay of the electromagnetic field and they also imply the existence of electromagnetic waves that we can describe by linear wave equation (here we use the form of equation in charge free space) [69]:

$$\Delta\mathbf{E} = \varepsilon\mu\frac{\partial^2 \mathbf{E}}{\partial t} \qquad \Delta\mathbf{B} = \varepsilon\mu\frac{\partial^2 \mathbf{B}}{\partial t}, \tag{3.3}$$

where Δ is a symbol for Laplace operator.

One of their solutions is a plane wave. Vectors $\mathbf{E}$ and $\mathbf{B}$ are perpendicular to each other and also to the direction of wave propagation as we can see in Figure 3.1. The sizes of vectors $\mathbf{E}$ and $\mathbf{B}$ satisfies equation $|\mathbf{E}| = v|\mathbf{B}|$,

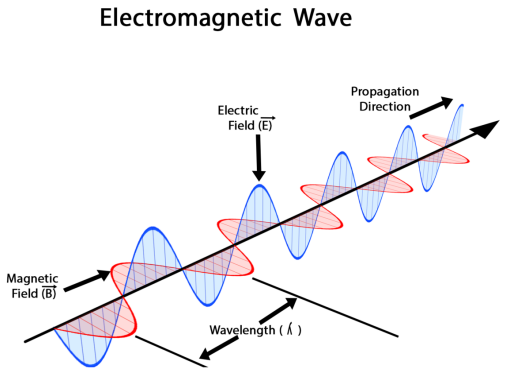

Figure 3.1: Scheme of the transverse electromagnetic wave, where the vectors **E** and **B** are perpendicular to each other and also to the direction of wave propagation [89].

where v is a velocity of propagation in given environment $v = 1/\sqrt{\varepsilon\mu}$ [68, 69].

The plane wave can be described by the course of the electric field intensity **E** [69]:

$$\mathbf{E}(\mathbf{r}, t) = \mathbf{E}_0 \cos(\omega t - \mathbf{k} \times \mathbf{r} + \varphi_0), \tag{3.4}$$

where $\mathbf{r} = (x, y, z)$ is vector of position, $\mathbf{E}_0$ is amplitude of electric field intensity, ω is angular frequency, $\mathbf{k}$ is wave vector and φ_0 is the phase of the wave. From Equation (3.4) is vector **B** clearly defined. All the important relation between related quantities we summerize in Equations (3.5-3.7) [69]:

$$T = \frac{2\pi}{\omega} \qquad \text{relation of period with angular frequency} \tag{3.5}$$

$$\lambda = vT \qquad \text{definition of wavelength of electromagnetic radiation} \tag{3.6}$$

$$k = |\mathbf{k}| = \frac{2\pi}{\lambda} \qquad \text{relation for the size of wave vector} \tag{3.7}$$

3.2 Polarization

In a plane perpendicular to the direction of wave propagation there are two independant transverse directions (determined by unit vectors $\mathbf{x}_0$ and $\mathbf{y}_0$) that we can consider as two independant polarization states [69]. Then, the monochromatic plane wave with angular frequency ω can be generally described (propagating along z axes) [69] as a superposition of waves oscillating in directions $\mathbf{x}_0$ and $\mathbf{y}_0$:

$$\mathbf{E}(z, t) = \mathbf{x}_0 E_1 \cos(\omega t - kz + \varphi_1) + \mathbf{y}_0 E_2 \cos(\omega t - kz + \varphi_2), \tag{3.8}$$

where aplitudes E_1,E_2 and phase constants φ_1 and φ_2 are indepandant constants. The most imporant types of polarization are two: linear and circular [68].

Linear polarization corresponds to situation, in which vector $\mathbf{E}(0,t)$[1] oscillates at the same direction, $\vartheta_1 - \vartheta_2 = 0$ or π and the ratio [69]:

$$\frac{E_x(0,t)}{E_y(0,t)} = \pm\frac{E_2}{E_1} = \tan\vartheta, \tag{3.9}$$

where ϑ is the angle from the x axes as it can be seen in Figure 3.2, remains constant.

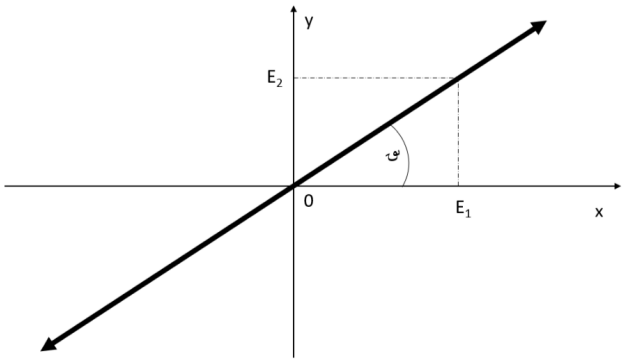

Figure 3.2: Linear polarization: $\mathrm{tg}\vartheta = E_2/E_1$.

Circular polarization corresponds to a situation, where $E_1 = E_2$, $\vartheta_1 - \vartheta_2 = \pm\frac{\pi}{2}$, and is a superposition of linear polarized waves in directions $\mathbf{x}_0$ and $\mathbf{y}_0$. Vector $\mathbf{E}(0,t)$ is moving around the cylinder of radius E_1 and we can distinguish left and right circularly polarized waves [68].

If we discuss reflection and transmission of waves, two orthogonal linear polarization states are the most important. P-polarized light has an electric field polarized parallel to the plane of incidence. S-polarized light is perpendicular to this plane, as we can see in Figure 3.3 [90].

[1] We set $z = 0$.

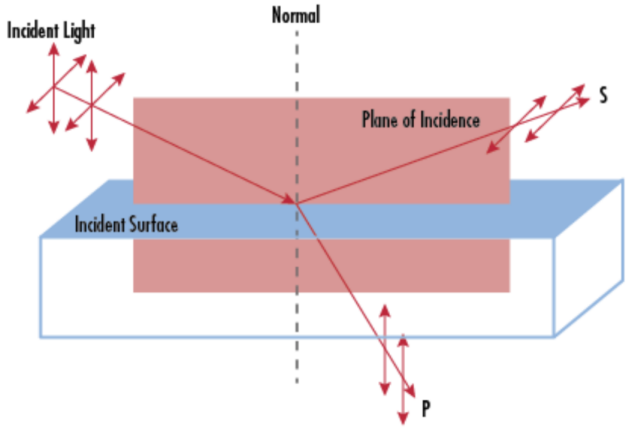

Figure 3.3: P-polarized and S-polarized light is defined by its relative orientation to the plane of incidence [90].

3.3 Interference

The most important quantity for the intereference description is the intensity of the electromagnetic radiations that is given by equation [69]:

$$I = \langle |E|^2 \rangle. \tag{3.10}$$

Let's consider two plane waves $\mathbf{E}_1$ and $\mathbf{E}_2$ with the same polarisation propagating in the same direction. If we consider the superposition $\mathbf{E} = \mathbf{E}_1 + \mathbf{E}_2$ that we can express intensity as [68]:

$$I = \langle |\mathbf{E}_1 + \mathbf{E}_2|^2 \rangle = \langle |\mathbf{E}_1|^2 \rangle + \langle |\mathbf{E}_2|^2 \rangle + 2|\mathbf{E}_0|^2 \langle \cos(\omega t - \mathbf{k}\cdot\mathbf{r} + \varphi_1) \cos(\omega t - \mathbf{k}\cdot\mathbf{r} + \varphi_2) \rangle \tag{3.11}$$

and if we put I_0 equal to intensity of wave $\mathbf{E}_1$ and $\Phi = \varphi_1 - \varphi_2$ then we have [69]:

$$I = 2I_0(1 + \cos\Phi), \tag{3.12}$$

because the time mean value of both waves is the same $I_0 = \frac{1}{2}|\mathbf{E}_0|^2$. Now let's consider two plane waves [69]:

$$\mathbf{E}_1(\mathbf{r}, t) = \mathbf{E}_0 \cos(\omega t - \mathbf{k}_1 \times \mathbf{r} + \varphi_1) \tag{3.13}$$

$$\mathbf{E}_2(\mathbf{r}, t) = \mathbf{E}_0 \cos(\omega t - \mathbf{k}_2 \times \mathbf{r} + \varphi_2) \tag{3.14}$$

with the same polarisation but different wave vectors[2] $\mathbf{k}_1$ and $\mathbf{k}_2$ that forms the angle ϑ.

[2] We consider that wave fronts of both waves are perpendicular to z-axes.

To get the distribution of the electromagnetic field in the chosen point $\mathbf{p} = (0, y, z)$ we have [69]:

- The superposition of both wave at point p is given by equation:

$$\mathbf{E}(\mathbf{p}, t) = \mathbf{E}_0 \cos(\omega t - ky \sin\vartheta_1 + \varphi_1) + \mathbf{E}_0 \cos(\omega t - ky \sin\vartheta_2 + \varphi_2). \quad (3.15)$$

- For the intensity of the resulting field, if the width difference d is given by the change in cosine function by 2π, we have:

$$I = 2I_0[1 + \cos(2\pi f_0 y + \Phi)], \quad (3.16)$$

  where f_0 is the frequency of the fringes given by $f_0 = 1/d$ and $\Phi = \varphi_1 - \varphi_2$ is the difference of initial phases.

- The width of fringes d is proportional to the angle ϑ between the plane waves and the relative position of the screen and wave vector $\mathbf{k} = \mathbf{k}_1 + \mathbf{k}_2$:

$$d \approx \frac{\lambda}{\Delta\vartheta \cos\vartheta}, \quad (3.17)$$

  where λ is the wavelength of the light we use, $\Delta\vartheta$ is the difference between angles ϑ_1 and ϑ_2 and $\vartheta = \frac{\vartheta_1 + \vartheta_2}{2}$. A a result we can expect wider fringes for longer wavelengths of used laser pulse [69].

3.4 Mach-Zehnder interferometer as a plasma diagnostic

Interferometers are one of the most common optical instruments, which are used for their ability of high precision measurements [83]. They split a (laser) beam into two components: a reference beam that travels unaltered through an optical path and a diagnostic beam traveling through a measured medium [85]. The interference of two or more electromagnetic waves can be achieved in two ways: by division of the wavefront (Fresnel, Lloyd interferometer) and by division of the amplitude (Mach-Zehnder, Michelson, Sagnack interferometer) [63].

Among the best known configurations of interferometers is the Mach-Zehnder interferometer. The laser beam is first split by a beamsplitter into two arms and then recombined by a second beamsplitter (see in Figure 3.4) [91]. Beamsplitters are generally pieces of glass with a dielectric coating on the front surface [92]. Laser striking it from the front site has a certain probability of being transmitted or reflected. On transmission a wave picks up no phase shift, a reflection induce a phase shift of π. If laser is approaching the beamsplitter

from behind, it first enters the glass and then has a certain probability of reflection within the glass - that reflection does not induce a phase change[3] [91]. If l_1 and l_2 are total path length from source to the detector for upper and lower paths according to Figure 3.4 and the light that passes through the beamsplitter picks up a phase shift of $2\pi t/\lambda$, where t is the optical path length throught the beamsplitter, then in total the upper path picks up the phase shift of [91]:

$$2\pi + 2\pi\left(\frac{l_1 + t}{\lambda}\right) \tag{3.18}$$

on the way to the detector A. Analogically we can express also the total phase shift for the lower path (see in Figure 3.4) on its way to the detector A. The phase difference between these two paths is [91]:

$$2\pi + 2\pi\left(\frac{l_1 + t}{\lambda}\right) - 2\pi - 2\pi\left(\frac{l_2 + t}{\lambda}\right) = 2\pi\left(\frac{l_1 - l_2}{\lambda}\right) = \delta, \tag{3.19}$$

where δ is the phase shift due to the difference in the path lengths. The same approach we can use for the path lengths to the detector B as we obtain:

$$2\pi + 2\pi\left(\frac{l_1 + 2t}{\lambda}\right) - \pi - 2\pi\left(\frac{l_2 + 2t}{\lambda}\right) = \pi + 2\pi\left(\frac{l_1 - l_2}{\lambda}\right) = \pi + \delta. \tag{3.20}$$

For $\delta = 0$, there is a constructive interference on the path to detector A and destructive to B. But the probability of arriving at either detector can be changed by varying δ [91]. This analysis is more complicated when different polarizations or wavelengths of laser are taken into account. While using this type of interferometer for measurements of plasma density, the laser beam passes through the target placed in the diagnostic arm only once. It therefore has half the sensitivity for the phase shift in comparison to Michaelson interferometer. On the other hand, the task of sharpening the resulting fringes is eliminated [61]. In addition, the reference beam is propagated along own path, hence it's not affected by the plasma.

Visualizing the temporal evolution of the plasma density distribution is important to understand the imploding dynamics. But the most of the interferometers work in the 'single-frame mode' [70], where only one shot is taken with the one laser beam passing through the plasma. If we take several 'single shots' in different times for different shots, we can map the evolution of the plasma implosion. Unfortunately, this method may be incorrect as the imploding of the dense magnetized plasma is usually not repeatable form shot to shot under the same experimental conditions [70]. The ideal solution would be designing of multi-frame interferometer capable of capturing several images within single shots.

[3] This rule is derived from the Fresnel equations for reflection and transmission of a wave at a dielectric [68].

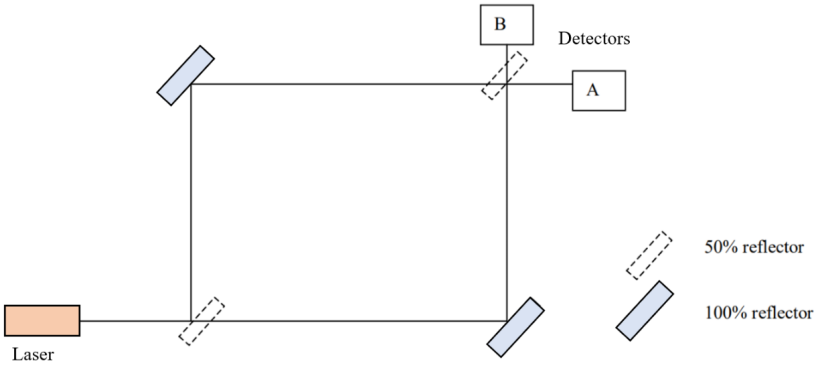

Figure 3.4: Mach-Zehnder interferometer: The laser beam is split by the first beamsplitter into a reference and a diagnostic arm and then recombined by the second one [91].

3.5 Fringe pattern analysis

Fringe images called interferograms are obtained during the interferometric measurements . Those interferograms can be described by [93]:

$$g(x,y) = a(x,y) + b(x,y)\cos[2\pi f_0 x + \Phi(x,y)], \tag{3.21}$$

where Φ is a phase term that carries the required information about the plasma density, x and y are the position variables and f_0 is the spatial-carrier frequency that characterized frequency of fringes in x direction. Functions $a(x,y)$ and $b(x,y)$ represent unwanted irradiance variations arising from the non-uniform light transmission of our plasma jet. Also functions $a(x,y)$, $b(x,y)$ and $\Phi(x,y)$ are changing slowly in comparison to f_0, so that is why it is possible to analyses those fringes to get desired information [93]. Using Euler equation for goniometric functions and setting $c(x,y) = \frac{1}{2}b(x,y)e^{i\Phi(x,y)}$ it is possible to rewrite the equation (3.21) into the form:

$$g(x,y) = a(x,y) + c(x,y)e^{2\pi f_0 x} + c^*(x,y)e^{-2\pi f_0 x}, \tag{3.22}$$

where * stands for complex conjugation.

If we use the Fourier transformation[4] to Equation (3.22) we get:

$$G(f,y) = A(f,y) + C(f - f_0, y) + C^*(f + f_0, y), \tag{3.23}$$

[4]Fourier transformation in 1D is a mapping defined as [94]:

$$F[h(x)](f) = \int_R h(x)e^{-2\pi i f x}\,\mathrm{d}x.$$

.

where G, A, C and C^* are Fourier images of initial functions. Variable f is the spatial frequency in the x direction. Since the spatial variation of a, b and Φ in x direction are slow compared to f_0, the Fourier images of our functions are separated exactly by the size of spatial-carrier frequency f_0 [93]. To extract the function $\Phi(x, y)$ we remove the left $C^*(f + f_0, y)$ and the middle $A(f, y)$ peak and move the right $C(f - f_0, y)$ to the center of the coordinate system, so we move it by f_0. Then we have a function $C(x, y)$ as we can see in Figure 4.1 and we can use inverse Fourier transformation to get $c(x, y)$ that we have defined earlier. Further we use arctangent[5] function to a quotient of the imaginary and the real part of the function $c(x, y)$ and we arrive to a relation for $\Phi(x, y)$. But this phase actually differs by factor of 2π from the real one. In most of the cases are all the measured values from the interval $(-\pi, \pi)$ so the next step of this process is to make the function continuous. One method for discontinuities correction is based on finding an offset phase distrobution $\Phi_0(x, y)$ that can be added to the discontinuos phase distribution Φ_d to convert it to continuos distribution $\Phi_c(x, y)$ [93]:

$$\Phi_c(x, y) = \Phi_d(x, y) + \Phi_0(x, y) \tag{3.24}$$

and is described in more detail in [93].

[5] We are using Euler equation $e^{i\varphi} = \cos\varphi + i\sin\varphi$.

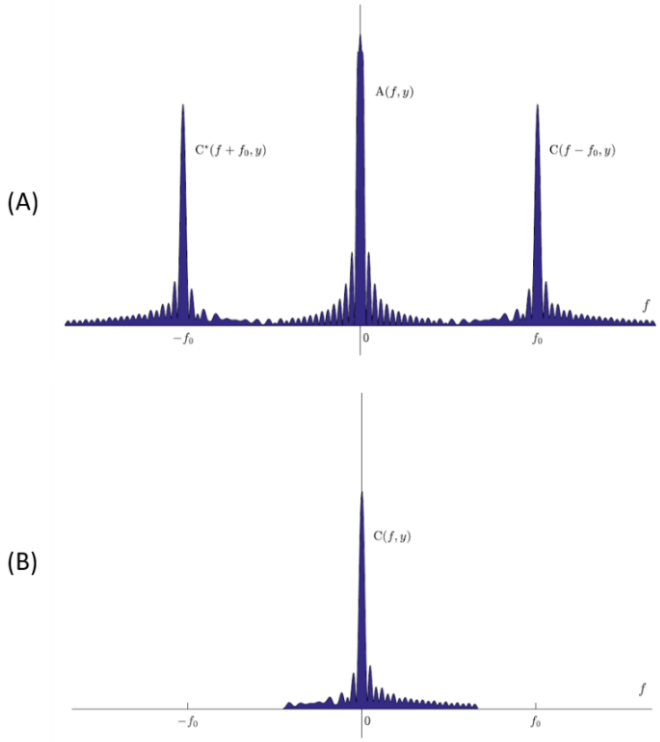

Figure 3.5: (A) Separated Fourier spectra of fringe pattern that are separated exactly by the size of spatial-carrier frequency f_0. (B) To extract the function $\Phi(x, y)$ we remove the left $C^*(f + f_0, y)$ and the middle $A(f, y)$ peak and move the right $C(f - f_0, y)$ to the center of the coordinate system [95].

Chapter 4

Experimental part

In this chapter we will introduce a novel concept of M-Z interferometer, which we designed and developed to study the plasma dynamics in single high-power laser shot. The proof of concept were made at Prague Asterix Laser System (PALS) before the experimental campaign focused on magnetic compressed jets carried out in December 2020. The obtained data and its analysis will be discussed.

4.1 Modified design of Mach-Zender interferometer

The four-frame Mach-Zender interferometer is sketched in Figure 4.1. The probe beam of two wavelengths firstly passed through the polarization cube and was split into two beams of different polarization (p is transmitted and s is reflected). Both beams then arrived in each path to dichroic mirrors, where higher wavelength was transmitted and lower reflected. That resulted in creation of four independent beams going through paths of different optical lengths. These paths (Delay 1-4 as it is shown in Figure 4.1.) were separated with a adjustable delay lines. All the independent beams were merged together with another set of dichroic mirrors and polarization cube and continued along the same path upto the M-Z interferometer. The interferograms were recorded on a four CCD cameras, where a combination of two lens system for image transmission was used to deliver a focused image of the plasma jet.

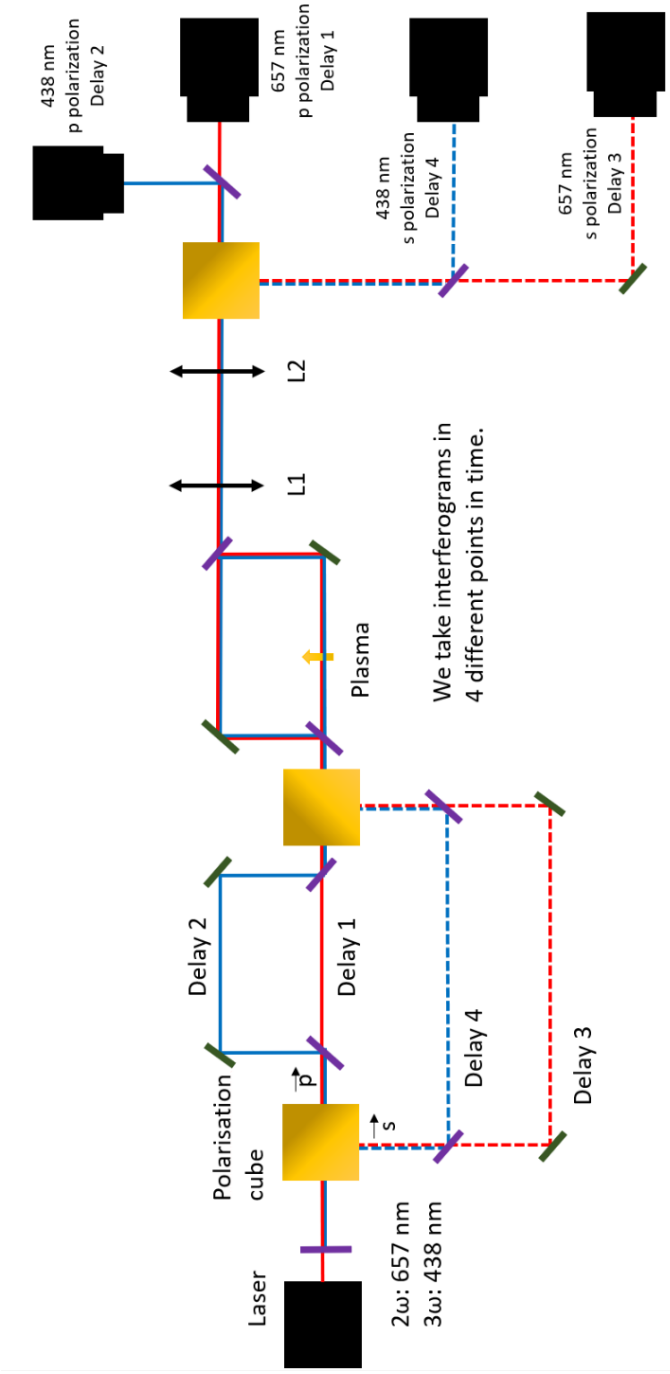

Figure 4.1: The scheme of four-frame M-Z interferometer with four adjustable delay lines.

4.1.1 Proof of concept

In order to successfully assemble the new four-beam M-Z interferometer, it was necessary to practically verify the new elements added to the basic set-up of the M-Z interferometer, especially the quality of the interference pattern on the detector after passing through a dichroic mirror or after passing through a polarization cube. Due to the typical dimensions of laboratory jets corresponding to mm scale, we also tried image transmission with magnification 1 for possible reduction or magnification of the plasma jet on the detector in the real experimental conditions. The proof of principle were made either with He-Ne laser or laser diodes emitting in visible region (see in Figure 4.2). As a target a grid or a gas nozzle with synthetic air were used. For simplicity we choose a Fresnel double prism ($\beta = 1.5°$) to create the fringe pattern.

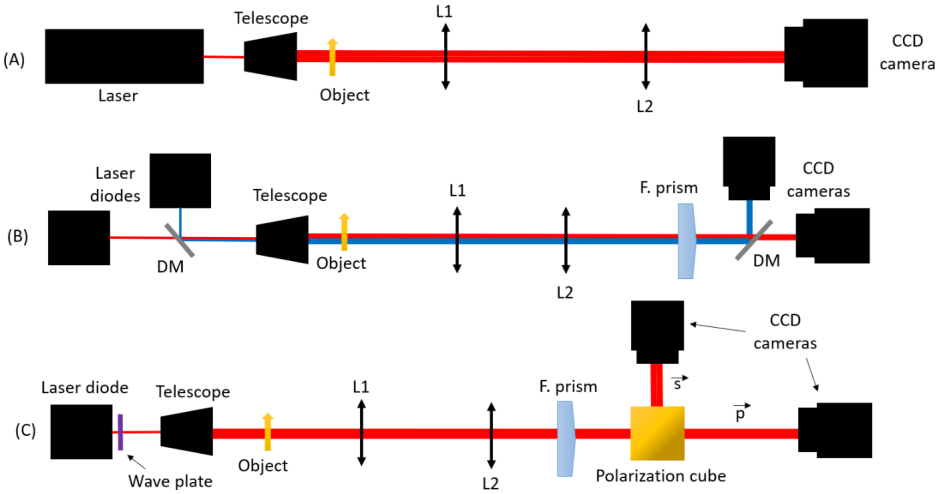

Figure 4.2: The scheme of the proof of concept measurements: (A) image transmisson, (B) imaging with two wavelengths, (C) imaging with two polarizations.

To try the imaging, we used system of two lenses with focal distance $f_1 = 300$ mm and $f_2 = 500$ mm, hence the object was placed at distance $2f_1$ and the image was formed at $2f_2$, the distance between lenses was $2|f_1 f_2|$. As a test object the grid (with 100 μm spacing) was used. The recorded image is nice and sharp in the central part, but due to final dimensions of the optical elements the outer part is blurred (see in Figure 4.3). Nevertheless, the horizontal and vertical spacing is 90 μm and its corresponding to magnification equal to 0,9. Before inserting the dichroic mirrors or polarization cube into the optical set-up, the Fresnel double prism was used to produce the interference pattern (see in Figure 4.4) and then the gas jet to make a displacement in the fringe pattern (see in Figure 4.5). The fringe shift corresponds to a different refractive index inside the gas.

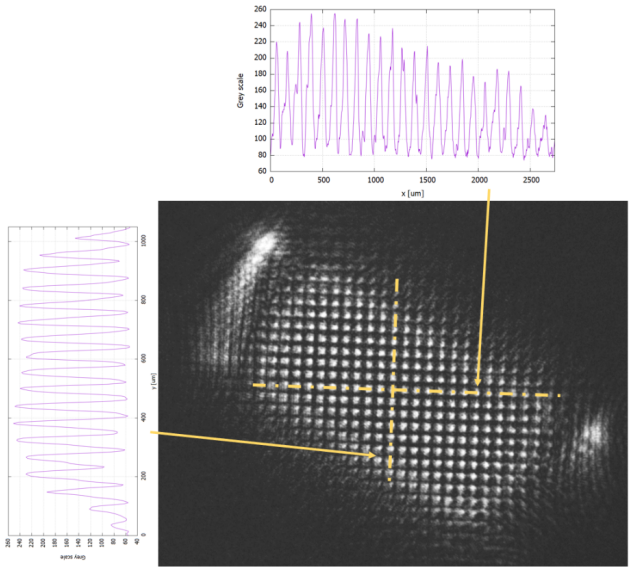

Figure 4.3: Image transmission by two lens system: Image of a grid.

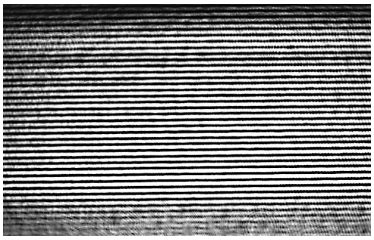

Figure 4.4: The interference pattern created by Fresnel interferometer.

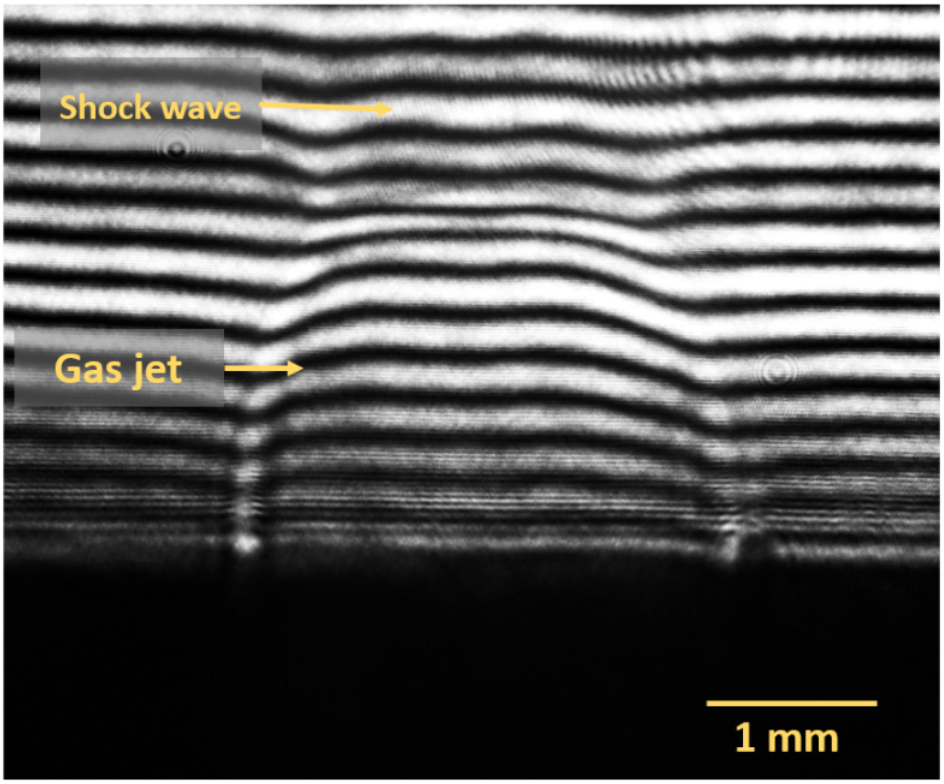

Figure 4.5: Interferogram of the gas jet. The shock wave can be also observed in the lower part of the image and the displacement of the fringes corresponds to a different refractive index inside the gas.

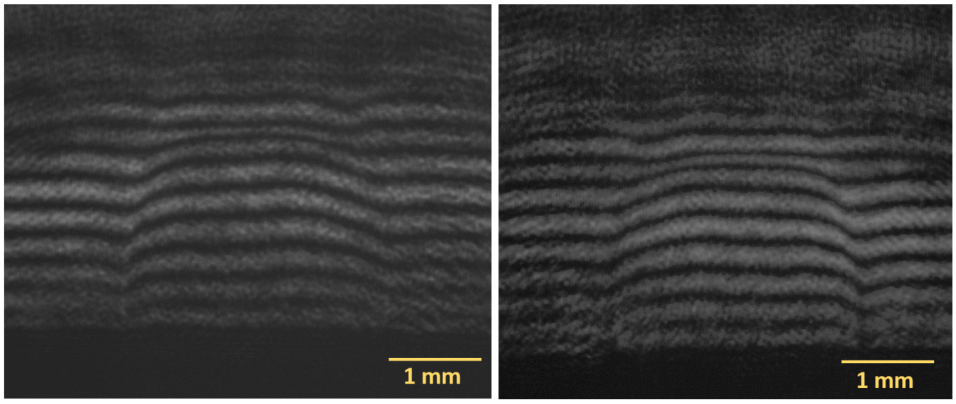

Figure 4.6: Interferogram of the gas jet for two different laser polarizations: (A) p polarization, (B) s polarization.

For the measurements with the polarization cube placed behind the double prism, the laser beam was divided to p and s polarization and the interference pattern was recorded on both cameras as it is shown in Figure 4.6. The results of the test with the dichroic mirror are shown in Figure 4.7, where two different laser wavelengths were used and as it is obvious the 'longer' red wavelength ($\lambda = 670$ nm) produce the larger fringe spacing than the 'shorter' blue wavelength ($\lambda = 450$ nm). The results of those tests prove that division of the primary laser beam to p and s polarization or transmission through the dichroic mirrors will not affect the information in the recorded interferograms.

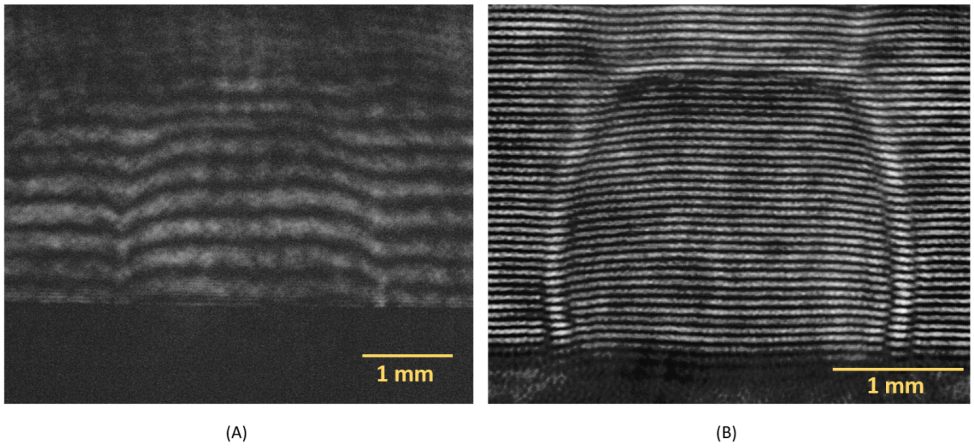

Figure 4.7: Interferogram of the gas jet for two different laser wavelengths: (A) red (670 nm), (B) blue (450 nm).

4.2 Experiment

The four-frame Mach-Zender interferometer was design and used as one of the diagnostics at PALS during the characterization of low-density rear-driven collisional plasma jets from thin foils. The motivation was to investigate the dynamics of colliding magnetised plasma jets that can be found around Active Galactic Nuclei or accreation discs and to build a platform to study transport properties on astrophysically relevant plasma that can be used in nuclear fusion experiment. The layout of the target area is pictured in Figure 4.8. The collisional rear-driven plasma jets were produced from the thin foil target as the kJ laser beam of 3ω irradiated it. The energy of the laser beam was around 200 J on target, pulse duration around 350 ps and the spot size 500 μm. The drive and the probe beam were carefully timed at the beginning of the experimental campaign to know the absolute value of the delay time, when the first probe beam was going through the jet. The other delay times were then calculated from the length difference of the delay lines and were possible to change between the shots.

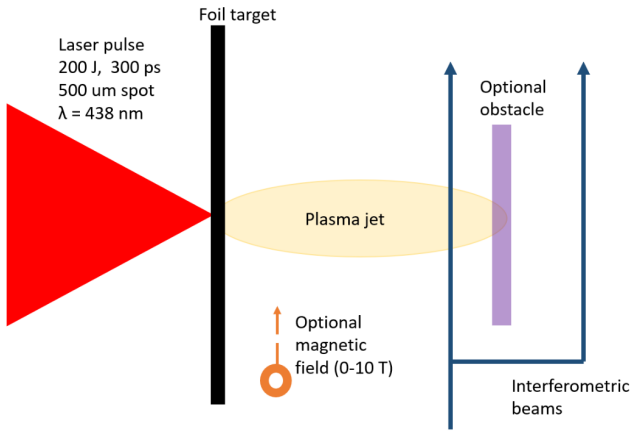

Figure 4.8: Layout of the target area with reference and diagnostic arms of the Mach-Zehnder interferometer.

The modified M-Z interferometer was used to measure the density evolution of plasma jets (images taken in four different times) that were made with 20 target variations (different material and thickness combination) that are shown in Figure 4.9. The diagnostics beamline was inferred from the main beam and hence splitted into two beams which were doubled (2ω at 657 nm) and tripled (3ω at 438 nm) in frequency (see in Figure 4.10). Those wavelengths corresponded to critical electron densities of $2,3 \times 10^{21}$ and $5,2 \times 10^{21}$ cm^{-3} up to which the probe beam theoretically could penetrate the plasma. The delay lines of adjustable length were situated on three separated optical tables, where

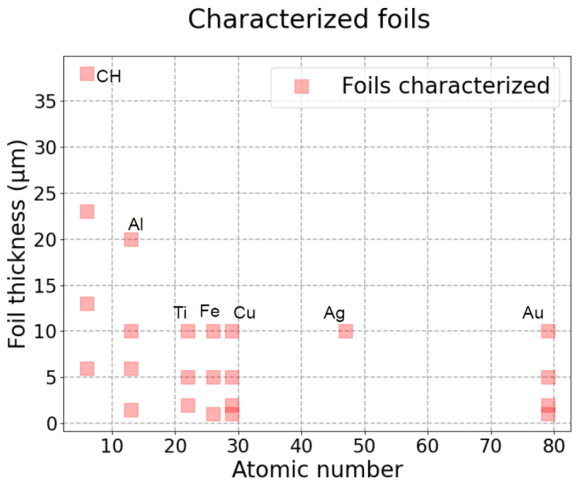

Figure 4.9: Available target materials that were used during the experiment.

two of them were movable to achieve longer delay times (see in Figure 4.11). As a result, the delays could be varied from 0 - 40 ns after the jet formation (the moment, when the drive beam irradiates the target).

The diagnostic and reference arm of the Mach-Zehnder interferometer were created by two 30:70 beamspitters. This coefficient was properly chosen so the beams that went through the different arms were of the same intensity at the end. The arms of the interferometer had to be of the same length as the pulse duration of the probe beam was around 350 ps and any length difference of more than 10,5 cm would not give any interference. The width of the interference fringes was adjusted to suitable size by the second beamsplitter.

The image transmission was provided by two lenses with focal lengths $F_1 = 300$ mm and $F_2 = 500$ mm with magnification of 2. As detectors, four 16 bits CCD (3376×2704 px, 1 px = 3,69 μm) cameras were used. Narrow band filters were placed before the cameras to depress the other wavelengths that could reach the camera. The resultant intensity of the interference images was created by Neutral Density (ND) filters before CCD cameras.

During the experiments we have overall performed 197 laser shots with three different cases studied: free jets, collisions with obstacles and magnetized jets. The target could be placed inside a pair of pulsed coil to study the effect of an external magnetic field of the strength of 5 - 15 T in direction perpendicular or parallel to the shock normal. As other plasma diagnostics, Streaked Optical Pyrometry (SOP) was used for tracking the jet expansion.

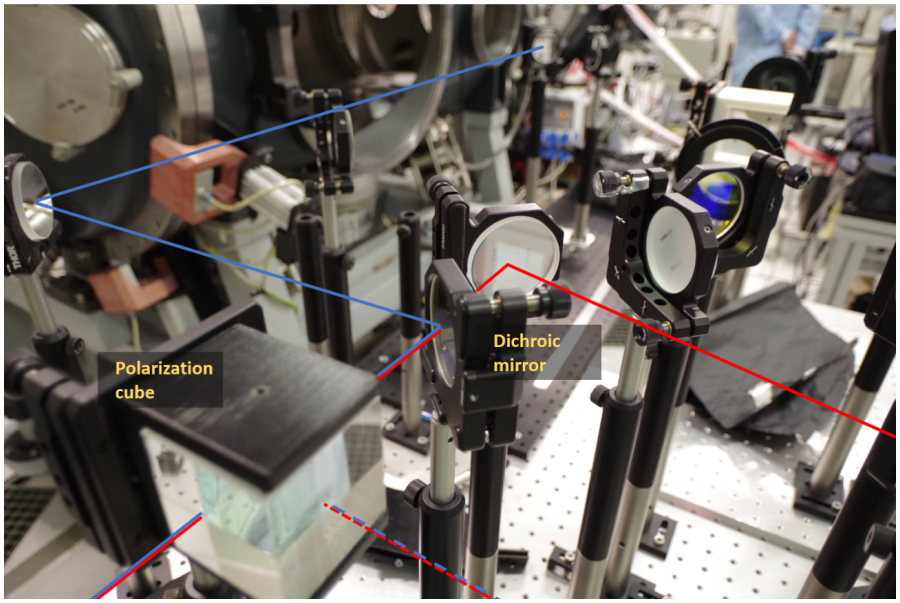

Figure 4.10: The probe beam was split by polarization cube to p (solid line) and s (dashed line) polarization and further by long-pass dichroic mirror to 'shorter' (blue line) and 'longer' (red line) wavelength.

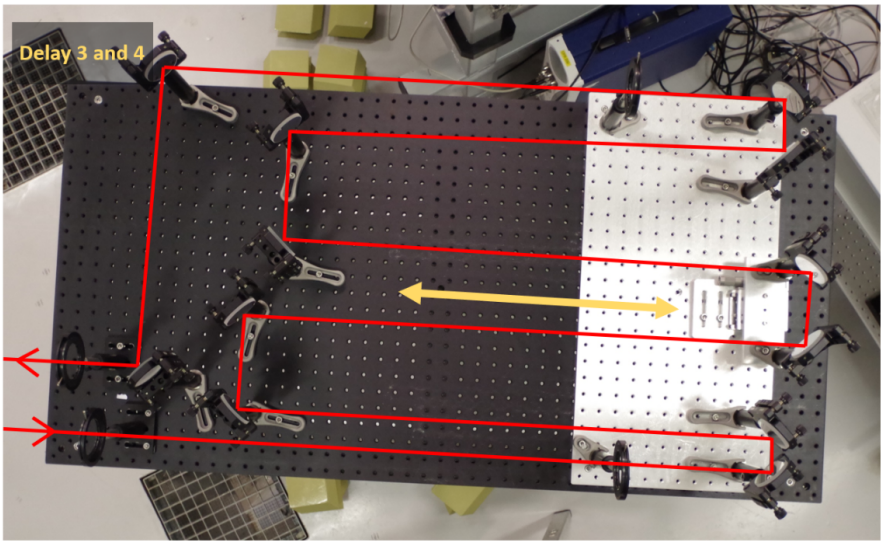

Figure 4.11: Delay lines 3 and 4 were situated on two movable tables that have allowed to achieve delays up to 40 ns after the jet formation. Yellow arrow indicates the possibility of adjusting the delay time just by moving the silver board on the table.

4.3 Results

Since the analysis of the interferogram is not simple process in this chapter will be presented only few results corresponding to three studied cases: free jet, magnetized jet, collision with obstacle.

The resulting set of images from 'four-frame mode' is shown in Figure 4.12, where set of four raw interferograms obtained within single shot can be seen.

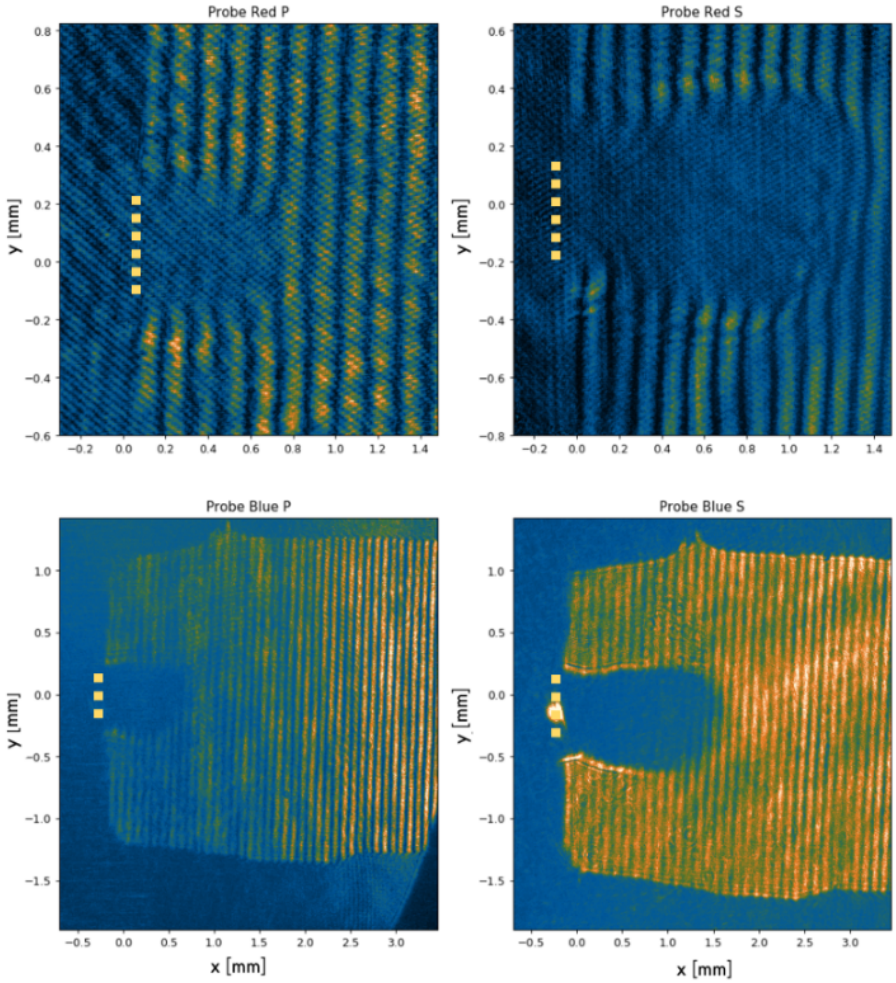

Figure 4.12: Set of images from 'four-frame mode' interferometer, which is obtained within single laser shot. The delay times after the jet formation are 10 ns (Red P), 13 ns (Blue P), 24 ns (Red S) and 25 ns (Blue S). The position of the target is indicated by yellow dotted line. The laser is incident from the left side.

Titanium foil of 10 μm thickness was used as a target. An example of plasma plum evaluation is recorded in times corresponding to 10 ns (Red

P), 13 ns (Blue P), 24 ns (Red S) and 25 ns (Blue S) after the jet formation. The position of the thin foil target is indicated by yellow dotted line, the drive beam is incident from the left side. The jet propagates from the left to the right and is symmetrical around the jet axes. The jet length is 0,5 mm in 10 ns and 1,5 mm in 25 ns after the jet formation. From the evolution of the jet length, we can estimate the jet velocity to be 66,6 μm/ns. The radial expansion of the jet is around 0,5 mm in 10 ns and 0,8 mm in 25 ns, so we can see that the jet preferential direction of propagation is along the jet axes. Right after the target we can see the area without intereference pattern, from where no probe light was recorded. It can be caused by the values of the density to be above the critical value or steep density gradients that refract the beam out of the collection optics.

A Python script was used to analysed the raw interferograms. For the analysis the cropped raw image was divided into two parts (along the horizontal coordinate) and by Fourier transform method (described in Chapter 3) two phase maps were retrieved (see in Figure 4.13).

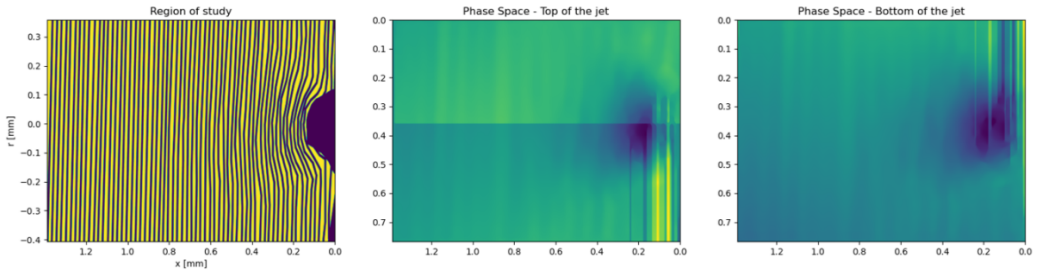

Figure 4.13: Fringe pattern analysis: At first, the phase maps of the top and bottom of the jet are created from the cropped raw image.

By combining phase maps from the top and bottom of the jet, we get the total phase map and at last the final density distribution (Figure 4.14). The position of 2 μm copper foil is indicated by yellow dotted line. The drive beam is incident from the right side and the jet propagates from the right to the left. The image is taken in 19 ns after the jet formation. Right after the target, the masked area can be seen as no interference pattern is recorded there. The possible reasons were discussed in the preceding paragraph. The highest density is measured in the central part of the jet, is equal to $3,0 \times 10^{19}$ cm^{-3} and lowers with the radial distance from the jet axes.

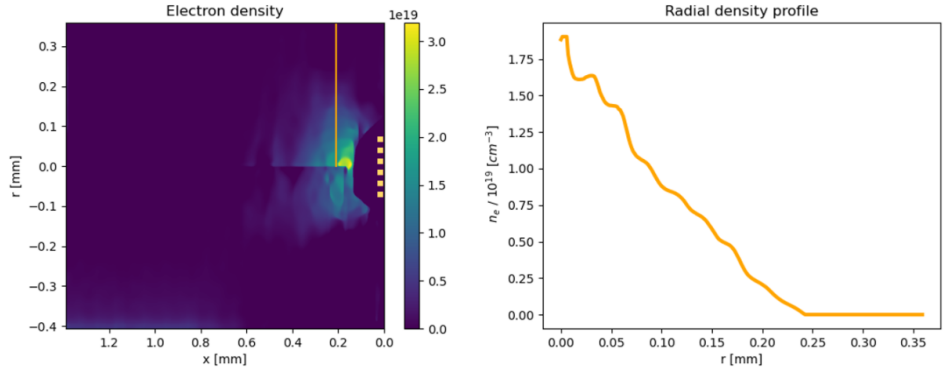

Figure 4.14: Density distribution of plasma jet: Cu target, thickness: 2 μm, delay: 19 ns. The target position is indicated by a yellow dotted line. The laser is incident from the right side.

If we take the whole set of four phase maps (see in Figure 4.15) in single shot, we can observe the density evolution of the jet in times 13 ns (Red P), 19 ns (Blue P), 25 ns (Red S), 33 ns (Blue S).

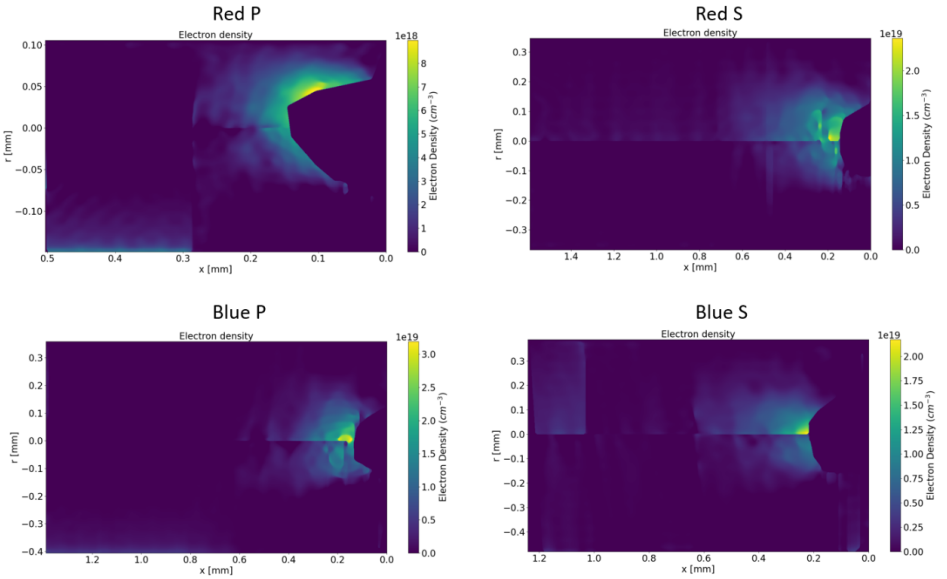

Figure 4.15: Density evolution of plasma jet: Cu target, thickness: 2 μm, delay: in times 13 ns (Red P), 19 ns (Blue P), 25 ns (Red S), 33 ns (Blue S). The target position is indicated by a yellow dotted line. The laser is incident from the right side.

In case of free jet propagation we used a different thickness of the material to create the plasma jets. The iron thin foils of 10 μm and 5 μm thickness were used and the retried phase maps can be seen in Figures 4.16 and 4.17. The

delay time was the same for both shots and equal to 36 ns. In case of a thicker foil in Figure 4.16, it can be seen that the radial expansion is smaller - around 0,2 mm, and for 5 μm foil, the radial expansion is 0,5 mm. The density is 3$\times$ higher in case of 10 μm foil as it reaches values of $3,5 \times 10^{19}$ cm^{-3} in the central part around the jet axes. The velocity of the jet is higher in case of 5μm foil and is 36 μm/ns. For 10μm target, it is 22 μm/ns.

Interferograms of plasma jet collisions with the wall (obstacle) were difficult to analyse. However, they are still usable for qualitative analysis. Here, we present a raw interferogram (see in Figure 4.18) of a 13 μm CH target at time of 22 ns after the jet formation. The wall was placed in the 2 mm distance from the target. The challenging part of the interferograms can be seen in the central part of the image, where the fringes start to connect itself due to the rebound of the plasma jet from the wall, so no n_e information can be obtained. The interferograms generally showed an increase in density in comparison to free jets. However, it is not clear, if it is due to compression effects, or just accumulated material. Further analysis will be needed to determine the cause.

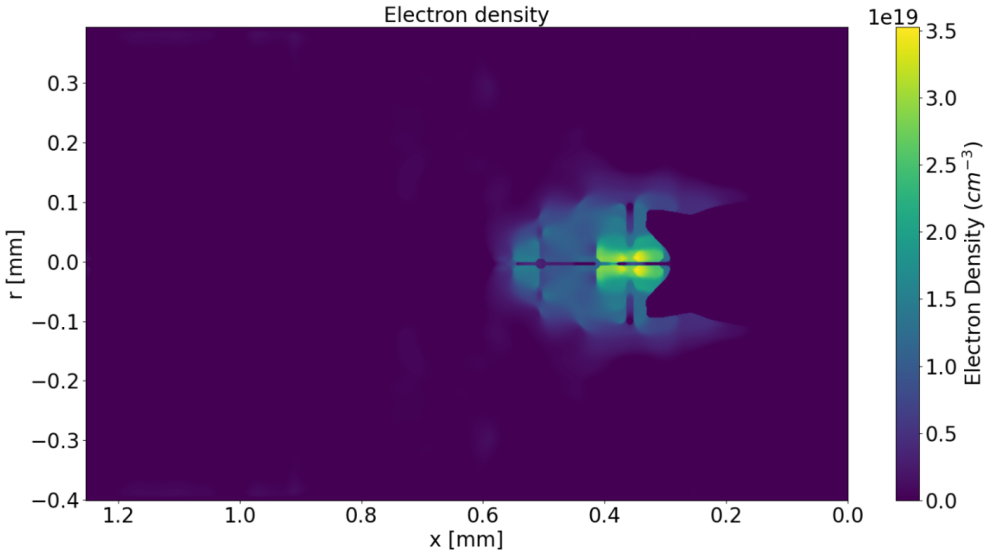

Figure 4.16: Density distribution of plasma jet: Fe target, thickness: 10 μm, delay: 36 ns.

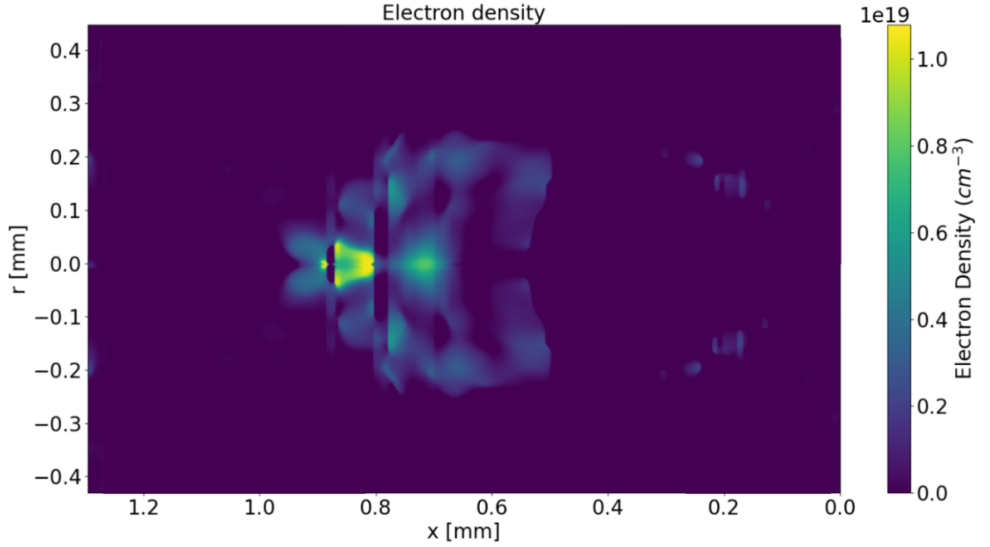

Figure 4.17: Density distribution of plasma jet: Fe target, thickness: 5 μm, delay: 36 ns.

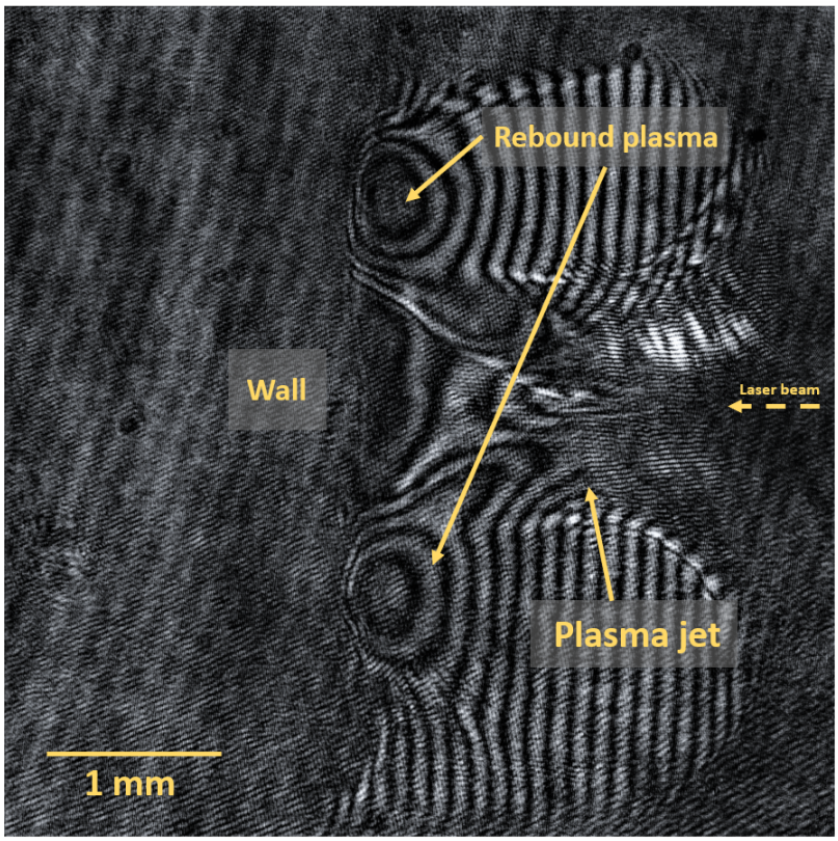

Figure 4.18: Interferogram of the plasma jet: CH target, thickness: 13 μm, delay: 22 ns, wall distance: 2 mm. The probe beam is coming from the left side. The laser is incident from the right side and the plasma jet is rebound from the wall.

The last case studied within the experimental campaign was to study the jet evolution under the influence of external magnetic field. In Figure 4.19, we present the phase map of the jet 34 ns after the jet formation from the 2 μm copper foil. The direction of the magnetic field of 10 T is parallel to the probe beam. The density of the jet is of the order 10^{19} cm^{-3} and is higher in the edges of the jet.

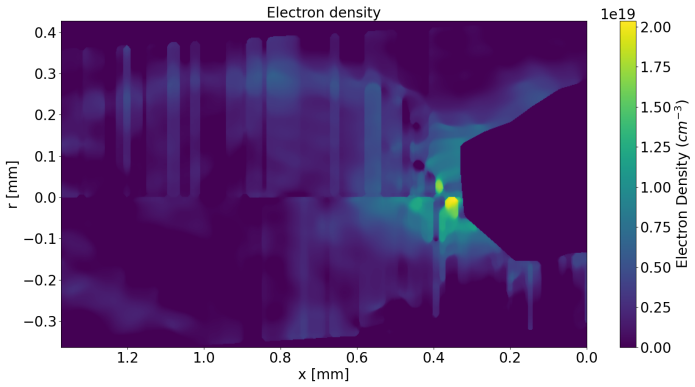

Figure 4.19: Magnetised jet: Cu target, thickness: 2 μm, delay: 34 ns, magnetic field: 10 T parallel to probe beam.

The effect of the external magnetic field is seen in the edges of the jet, which gets collimated. That can be caused by dominance of magnetic pressure over plasma pressure. This effect is more clear, when we probe in the field direction (see in Figure 4.20(A)) and the magnetic force is perpendicular to both fields and jet velocity, than in case of probing perpendicular to the field direction (see in Figure 4.20(B)). Further calculations of β_{ram} will be needed to understand the effect.

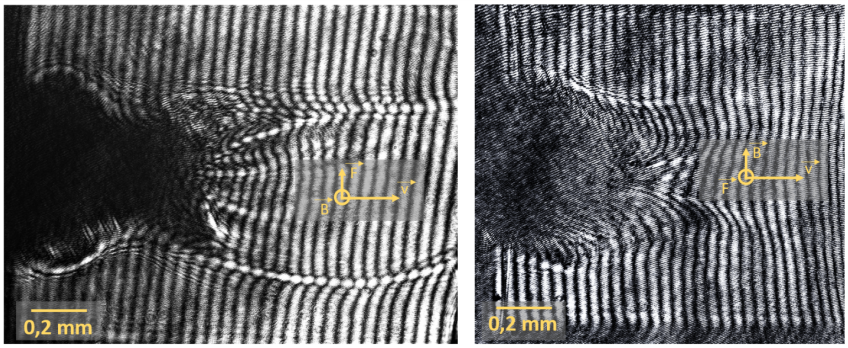

Figure 4.20: Magnetised jet: Al target, thickness: 6 μm, delay: 28 ns (A) and 40 ns (B), magnetic field: 10 T parallel (A) and perpendicular to probe beam (B).

4.3.1 Modification to four-frame shadowgraphy

During the experimental campaign we realized that by simple modification of the interferometer we can simultaneously use the set-up for the shadowgraphy. By adding beamsplitter after the target, we split the diagnostic beam and part was send to interefometer and the rest was used for the shadowgraphy (see in Figure 4.21). Further the beams were divided by polarization cube to s and p polarization and by dichroic mirrors we separated the 2ω and 3ω. To image interesting part of the jet we used a magnification lens L_2. The results are shown in Figure 4.22, where in single shot we recorded both interferograms (see in Figure 4.22(A) and shadowgraphs (see in Figure 4.22(B)).

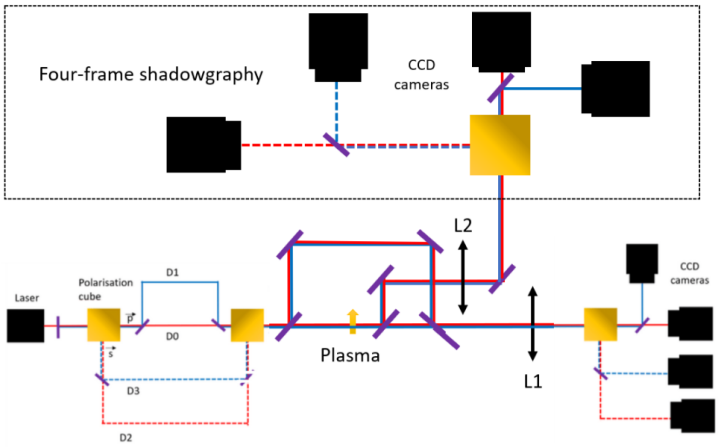

Figure 4.21: The layout of the interferometer modification. Four-frame shadowgraphy set-up is added.

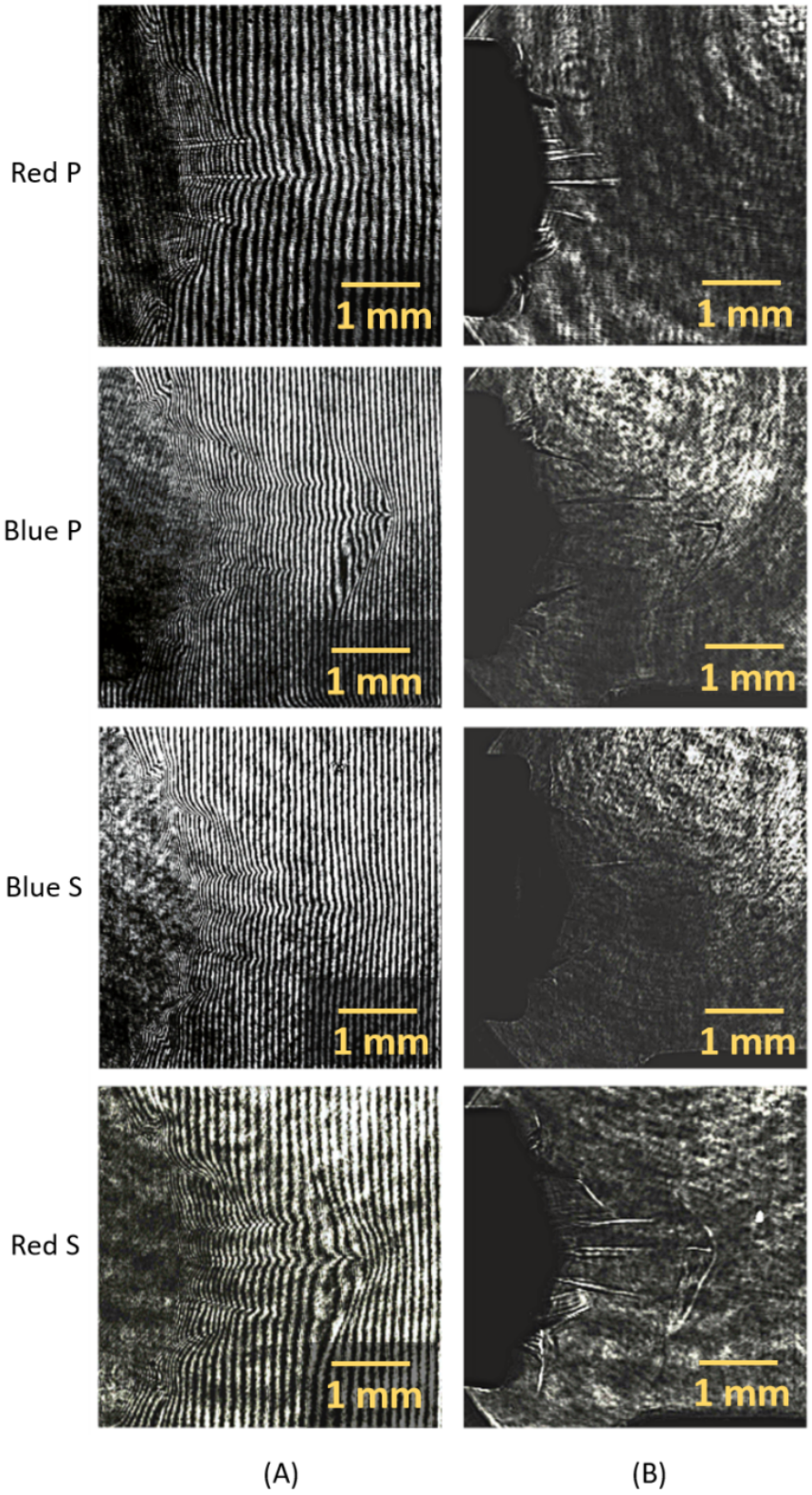

Figure 4.22: Preliminary results: Complete set of 8 images: four-frame interferometry in the left column, four-frame shadowgraphy in the right column.

Conclusion

This work is dedicated to physics of astrophysical jets and possible scaling of dynamical processes in laboratory conditions. These jets, that can be formed by for example Active Galactic Nucleis, may be responsible for the acceleration of particles to the highest energies.

In this thesis, I have compiled the necessary knowledge for studying the magnetized plasma jets in laboratory conditions. These findings served me as a solid basis for designing the concept of four-frame Mach-Zehnder interferometer, which consists of splitting the probe beam by its polarization and wavelength, and is an unique instrument for plasma jet density evolution measurements. Further, I have successfully conducted proof of concepts measurements to test the functionality of image transformation and interferometry imaging for beams of different wavelengths and polarizations. Hereafter, I have installed the four-frame Mach-Zehnder interferometer at Prague Asterix Laser System laboratory, collected and analysed data from the plasma jet experiment. The advantages of the interferometer are easily adjustable delays, high stability and fast installation. In addition, compared to existing studies with wavefront division interferometers, the advantage of the M-Z interferometer is that the reference beam is propagated along own path, hence it's not affected by the plasma.

The shots with free jets show the dependence of the jet density and shape on the chosen target material and its thickness. In case of 10 μm thicker foil, the radial expansion was smaller - around 0,2 mm, and for 5 μm foil, the radial expansion was 0,5 mm. The density was 3$\times$ higher in case of 10 μm foil as it reaches values of $3,5 \times 10^{19}$ cm^{-3} in the central part around the jet axes. The velocity of the jet was higher in case of 5μm foil and was equal to 36 μm/ns. For 10μm target, it is 22 μm/ns. Interferograms of plasma jets collisions with the wall were of the challenge to the analysis, but are good for qualitative analysis. The interferograms generally showed higher density values in comparison to free jets and further analysis is needed to determine the cause. The effect of external magnetic field was observed at the edges of the jets as they got more collimated in both cases of probing parallel and perpendicular to the field direction. Further calculations of β_{ram} will be needed to understand the effect.

Beyond the assignment of this master's thesis, I have improved the four-frame interferometer by adding four-frame shadowgraphy into the design. The 'eight-frame' regime was also successfully tested in the experiment.

My future plans are to continue with the analysis of experimental results and further investigate the options of multi-frame plasma diagnostics, such as interferometry and shadowgraphy, but also polarimetry or their combinations in astrophysical measurements that can lead to better understanding of plasma dynamics and transport properties.

Bibliography

[1] Gregory G. Howes. "Laboratory space physics: Investigating the physics of space plasmas in the laboratory". In: *Physics of Plasmas* 25.5 (2018), p. 055501. DOI: 10.1063/1.5025421.

[2] D. C. Ellison, A. Decourchelle, and J. Ballet. "Nonlinear particle acceleration at reverse shocks in supernova remnants". In: *Astronomy and Astrophysics* 429.2 (2004), pp. 569–580. DOI: 10.1051/0004-6361:20041668.

[3] *Astrophysics*. Available online: https://www.wikiwand.com/en/Astrophysics.

[4] James E. Keeler. "The Importance of ASTROPHYSIC4L Research and the Relation of Astrophysics to Other Physical Sciences." In: *The Astrophysical Journal* 6 (1897), p. 271. DOI: 10.1086/140401.

[5] C. Grupen. *Astroparticle Physics*. Springer, 2005.

[6] Dan Maoz. *Astrophysics in a Nutshell: Second Edition*. PRINCETON UNIV PR, Feb. 23, 2016. 312 pp. ISBN: 0691164797. URL: https://www.ebook.de/de/product/24977394/dan_maoz_astrophysics_in_a_nutshell_second_edition.html.

[7] M. Longair. *High energy astrophysics*. Cambridge University Press, 1981.

[8] V. Hess. "Uber Beobachtungen der durchdringenden Strahlung bei sieben Freiballonfahrten". In: *Phys.Z.* (1912).

[9] *Cosmic rays: particles from outer space*. Available online: https://home.cern/science/physics/cosmic-rays-particles-outer-space. 2022.

[10] A. D. Erlykin and A. W. Wolfendale. "The Origin of the Knee in the Cosmic Ray Energy Spectrum". In: *Astro.Ph.* (Mar. 28, 2001). arXiv: http://arxiv.org/abs/astro-ph/0103477v2 [astro-ph].

[11] Michael Unger, Glennys R. Farrar, and Luis A. Anchordoqui. "Origin of the ankle in the ultrahigh energy cosmic ray spectrum, and of the extragalactic protons below it". In: *Physical Review D* 92.12 (2015). DOI: 10.1103/physrevd.92.123001.

[12] *GZK limit*. Available online: http://astro.vaporia.com/start/gzklimit.html.

[13] Pijushpani Bhattacharjee and Günter Sigl. "Extreme Energy Cosmic Rays: Hints to New Physics Beyond the Standard Model?" In: *Physics and Astrophysics of Ultra-High-Energy Cosmic Rays*. Springer Berlin Heidelberg, 2015, pp. 275–299. DOI: 10.1007/3-540-45615-5_11.

[14] N. Wolchover. *The Particle That Broke a Cosmic Speed Limit*. Available online: https://www.quantamagazine.org/ultrahigh-energy-cosmic-rays-traced-to-hotspot-20150514. 2015.

[15] T. Bridgman. *Shock Drift Acceleration*. Available online: https://svs.gsfc.nasa.gov/4513. 2016.

[16] P. Kulhanek. *Uvod do teorie plazmatu*. AGA, 2017.

[17] J. Vicha. *Zdroje a urychlovani kosmickeho zareni*. Available online: https://www.fzu.cz/~vicha/lectures/2021-2022/07-Astrocastice_zdroje_2021.pdf. 2021.

[18] P. Louarn. *Acceleration in magnetospheres*. ESA Publications Division, 2002.

[19] A. Velasquez. *High-energy cosmic-ray acceleration*. en. 2010. DOI: 10.5170/CERN-2010-001.533.

[20] Frank C. Jones. "A theoretical review of diffusive shock acceleration". In: *The Astrophysical Journal Supplement Series* 90 (1994), p. 561. DOI: 10.1086/191875.

[21] P. A. Sturrock. "Stochastic Acceleration". In: *Physical Review* 141.1 (1966), pp. 186–191. DOI: 10.1103/physrev.141.186.

[22] Siming Liu and J. Randy Jokipii. "Acceleration of Charged Particles in Astrophysical Plasmas". In: *Frontiers in Astronomy and Space Sciences* 8 (2021). DOI: 10.3389/fspas.2021.651830.

[23] Lewis Ball and D. B. Melrose. "Shock Drift Acceleration of Electrons". In: *Publications of the Astronomical Society of Australia* 18.4 (2001), pp. 361–373. DOI: 10.1071/as01047.

[24] P. Lagage. "The maximum energy of cosmic rays accelerated by supernova shocks". In: *Astronomy and Astrophysics* (1983).

[25] Roger Blandford, David Meier, and Anthony Readhead. "Relativistic Jets in Active Galactic Nuclei". In: *Astro.Ph.* (Dec. 14, 2018). DOI: 10.1146/annurev-astro-081817-051948. arXiv: http://arxiv.org/abs/1812.06025v1 [astro-ph.HE].

[26] Donald C. Ellison, Eberhard Moebius, and Goetz Paschmann. "Particle injection and acceleration at earths bow shock - Comparison of upstream and downstream events". In: *The Astrophysical Journal* 352 (1990), p. 376. DOI: 10.1086/168544.

[27] *Binary star systems: Classification and Evolution*. Available online: https://www.space.com/22509-binary-stars.html. 2018.

[28] Siyao Xu and Alex Lazarian. "Shock acceleration with oblique and turbulent magnetic fields". In: *Astr.Ph.* (Nov. 8, 2021). DOI: 10.3847/1538-4357/ac3824. arXiv: http://arxiv.org/abs/2111.04759v1 [astro-ph.HE].

[29] G. Livadiotis. "Rankine Hugoniot Shock Conditions for Space and Astrophysical Plasmas Described by Kappa Distributions". In: *The Astrophysical Journal* 886.1 (2019), p. 3. DOI: 10.3847/1538-4357/ab487a. URL: https://doi.org/10.3847/1538-4357/ab487a.

[30] M. Aartsen. "Astrophysical neutrinos and cosmic rays observed by IceCube". In: *Advances in Space Research* 62.10 (2018), pp. 2902–2930. DOI: 10.1016/j.asr.2017.05.030.

[31] F. Aharonian. *Hillas Plot: trivial and non trivial implications*. Available online: https://www.mpi-hd.mpg.de/hillas2018/slides/Hillas2018_07_Aharonian.pdf. 2018.

[32] Britannica. *pulsar*. Available online: https://www.britannica.com/science/pulsar. 2022.

[33] G. Setti. *Origin of Cosmic Rays*. SPRINGER NATURE, May 31, 1981. 409 pp. ISBN: 9027712719. URL: https://www.ebook.de/de/product/2060910/origin_of_cosmic_rays.html.

[34] Claire Guepin, Benoit Cerutti, and Kumiko Kotera. "Proton acceleration in pulsar magnetospheres". In: *Astronomy and Astrophysics* 635 (2020), A138. DOI: 10.1051/0004-6361/201936816.

[35] The Pierre Auger Collaboration. "Correlation of the highest-energy cosmic rays with the positions of nearby active galactic nuclei". In: *Astropart.Phys.* (Dec. 17, 2007). DOI: 10.1016/j.astropartphys.2008.01.002. arXiv: http://arxiv.org/abs/0712.2843v2 [astro-ph].

[36] D. Fargion and A. Colaiuda. "Gamma rays precursors and afterglows surrounding UHECR events: Z-burst model is still alive". In: *Nuclear Physics B. (Proc. Suppl.) 136 (2004) 256-262* (Sept. 1, 2004). DOI: 10.1016/j.nuclphysbps.2004.10.009. arXiv: http://arxiv.org/abs/astro-ph/0409022v2 [astro-ph].

[37] Thomas J. Weiler. "Relic Neutrinos, ZBursts, and Cosmic Rays above 1020 eV". In: *Astro.Ph.* (Oct. 13, 1999). arXiv: http://arxiv.org/abs/hep-ph/9910316v1 [hep-ph].

[38] L. Hronova. "Zkouman vzniku energetickych castic urychlenych v plazmovych vytryscch generovanych vysokoenergetickym laserovym impulzem". MA thesis. Czech Technical University, 2020.

[39] M. Goossens. *An Introduction to Plasma Astrophysics and Magnetohydrodynamics*. Heverlee, 2003.

[40] *Laboratory astrophysics*. Available online: https://www.plasma-universe.com/laboratory-astrophysics/. 2022.

[41] James Matthews, Anthony Bell, and Katherine Blundell. "Particle acceleration in astrophysical jets". In: *Astro.Ph.* (Mar. 14, 2020). DOI: 10.1016/j.newar.2020.101543. arXiv: http://arxiv.org/abs/2003.06587v1 [astro-ph.HE].

[42] *Galactic jets*. Available online: https://astronomy.swin.edu.au/cosmos/g/GalacticJets. 2022.

[43] C. Gregory. "Astrophysical jet experiments". In: *Plasma Physics and Controlled Fusion* 50.12 (2008), p. 124039. DOI: 10.1088/0741-3335/50/12/124039.

[44] Robert M. Jeffrey et al. "Fast launch speeds in radio flares, from a new determination of the intrinsic motions of SS 433s jet bolides". In: *Monthly notices of the Royale astronomical society* (June 3, 2016). DOI: 10.1093/mnras/stw1322. arXiv: http://arxiv.org/abs/1606.01240v1 [astro-ph.HE].

[45] Y. Minami. "New development of space propulsion theory: breakthrough of concentional propulsion theory". In: *International journal of advanced engineering and management research* (2019).

[46] D. Tordella. "Focul on astrophysical jets". In: *IOP Publishing* (2015).

[47] A. Diziere et al. "Formation and propagation of laser driven plasma jets in an ambient medium studied with Xray radiography and optical diagnostics". In: *Physics of Plasmas* 22.1 (2015), p. 012702. DOI: 10.1063/1.4905525.

[48] A. Tonomura. *The double slit experiment*. Available online: https://physicsworld.com/a/the-double-slit-experiment/. 2022.

[49] J. Biteau et al. "Progress in unveiling extreme particle acceleration in persistent astrophysical jets". In: *Nature Astronomy* 4.2 (2020), pp. 124–131. DOI: 10.1038/s41550-019-0988-4.

[50] Bradford Snios et al. "Variability and Proper Motion of X-Ray Knots in the Jet of Centaurus A". In: *The Astrophysical Journal* 871.2 (2019), p. 248. DOI: 10.3847/1538-4357/aafaf3.

[51] Frank M. Rieger and Peter Duffy. "Shear Acceleration in Relativistic Astrophysical Jets". In: *The Astrophysical Journal* 617.1 (2004), pp. 155–161. DOI: 10.1086/425167.

[52] J. F. Drake et al. "A computational model for exploring particle acceleration during reconnection in macro-scale systems". In: *Astro.Ph.* (Sept. 12, 2018). DOI: 10.1063/1.5058140. arXiv: http://arxiv.org/abs/1809.04568v3 [astro-ph.SR].

[53] Raffaella Margutti et al. "The Binary Neutron Star event LIGO VIRGO GW170817 a hundred and sixty days after merger: synchrotron emission across the electromagnetic spectrum". In: *The Astrophysical journal letters* (Jan. 10, 2018). DOI: 10.3847/2041-8213/aab2ad. arXiv: http://arxiv.org/abs/1801.03531v2 [astro-ph.HE].

[54] P. Chen. "Laser cosmology". In: *The European Physical Journal Special Topics* 223.6 (2014), pp. 1121–1129. DOI: 10.1140/epjst/e2014-02163-5.

[55] P. Maine et al. "Generation of ultrahigh peak power pulses by chirped pulse amplification". In: *IEEE Journal of Quantum Electronics* 24.2 (1988), pp. 398–403. DOI: 10.1109/3.137.

[56] Daniel Wolf Savin et al. "Laboratory Astrophysics White Paper". In: *NASA Laboratory Astrophysics Workshop* (Mar. 7, 2011). arXiv: http://arxiv.org/abs/1103.1341v1 [astro-ph.IM].

[57] T. Zh. Esirkepov and S. V. Bulanov. "Fundamental Physics and Relativistic Laboratory Astrophysics with Extreme Power Lasers". In: *EAS Publications Series 58, pp 7-22 (2012)* (Feb. 21, 2012). DOI: 10.1051/eas/1258001. arXiv: http://arxiv.org/abs/1202.4552v1 [astro-ph.HE].

[58] S. V. Bulanov et al. "On the problems of relativistic laboratory astrophysics and fundamental physics with super powerful lasers". In: *Plasma Physics Reports* 41.1 (2015), pp. 1–51. DOI: 10.1134/s1063780x15010018.

[59] Y. Zakharov. "Collisionless laboratory astrophysics with lasers". In: *IEEE transactions od plasma science* (2003).

[60] Katerina Falk. *Plasma Physics*. Prednaska. 2020.

[61] P. Fiala. *Fyzikalni optika*. Vydavatelstvi CVUT, 2005. ISBN: 80-01-03183-7.

[62] J. A. Bittencourt. *Fundamentals of Plasma Physics*. Springer New York, 2004. DOI: 10.1007/978-1-4757-4030-1.

[63] S. S. Harilal and M. S. Tillack. *Laser plasma density measurements using interferometry*. Dostupne z: https://cer.ucsd.edu/_files/publications/UCSD-ENG-114.pdf. 2004.

[64] M. V. del Valle, A. Araudo, and F. Suzuki-Vidal. "Adiabatic radiative shock systems in YSO jets and novae outflows". In: *Astro.Ph.* (Jan. 5, 2022). arXiv: http://arxiv.org/abs/2201.01696v1 [astro-ph.HE].

[65] Andrea Ciardi. "Laboratory Studies of Astrophysical Jets". In: *Lect.Notes Phys.793:31-50,2010* (Mar. 2, 2009). DOI: 10.1007/978-3-642-02289-0_2. arXiv: http://arxiv.org/abs/0903.0268v1 [astro-ph.SR].

[66] X. Ribeyre et al. "Simulations of the supersonic radiative jet propagation in plasmas". In: *Astrophysics and Space Science* 322.1-4 (2008), pp. 85–90. DOI: 10.1007/s10509-008-9936-y.

[67] P. Antici. "Time and space resolved interferometry for laser generated fast electron measurements". In: *Review of Scientific Instruments* (2010).

[68] E. Hecht. *Optics*. Addison Wesley, 2002. ISBN: 0-321-18878-0.

[69] J. Tolar. *Vlneni, optika a atomova fyzika*. Available online: https://physics.fjfi.cvut.cz/~schmidt/voaf/utrzkyVOAF.pdf. 2017.

[70] Xinxin Wang et al. "A three-frame Mach Zehnder interferometer for measuring dense magnetized plasmas". In: *Review of Scientific Instruments* 74.3 (2003), pp. 1328–1331. DOI: 10.1063/1.1540720.

[71] B. Albertazzi et al. "Experimental platform for the investigation of magnetized reverse shock dynamics in the context of POLAR". In: *High Power Laser Science and Engineering* 6 (2018). DOI: 10.1017/hpl.2018.37.

[72] L. Van Box Som et al. "Laboratory radiative accretion shocks on GEKKO XII laser facility for POLAR project". In: *Astr.Ph.* (2018). arXiv: http://arxiv.org/abs/1804.02714v1 [astro-ph.HE].

[73] E. Parker. *Principles of Magnetohydrodynamics, with Applications to Laboratory and Astrophysical Plasma*. Cambridge university press, 2004.

[74] É. Falize, C. Michaut, and S. Bouquet. "SIMILARITY PROPERTIES AND SCALING LAWS OF RADIATION HYDRODYNAMIC FLOWS IN LABORATORY ASTROPHYSICS". In: *The Astrophysical Journal* 730.2 (2011), p. 96. DOI: 10.1088/0004-637x/730/2/96.

[75] R. Shishoo. *Plasma technologies for textiles*. Woodhead Publishing in textiles, 2007. ISBN: 978-1-84569-073-1.

[76] I. Hutchinson. *Principles of plasma diagnostics*. Cambridge University Press, 2022. ISBN: 978-0-521-80389-2.

[77] Lukas Schmiedt and Mojmir Jilek. *Diagnostiky plazmatu*. Dostupne z: `https://physics.mff.cuni.cz/kfpp/s4r/plazma/?p=2`. 2020.

[78] C. Mendel. "Plasma Diagnostic Techniques". In: *the Encyclopedia of Physical Science and Technology* (2002).

[79] M. N. Shneider and R. B. Miles. "Microwave diagnostics of small plasma objects". In: *Journal of Applied Physics* 98.3 (2005), p. 033301. DOI: `10.1063/1.1996835`.

[80] R. A. Gottscho and T. A. Miller. "Optical techniques in plasma diagnostics". In: *Pure and Applied Chemistry* 56.2 (1984), pp. 189–208. DOI: `10.1351/pac198456020189`.

[81] B. Rowe. "A mass spectrometer for plasma diagnostics. Measurements of ion translational temperature, polarization and velocity effects". In: *International Journal of Mass Spectrometry and Ion Physics* 16.3 (1975), pp. 209–223. DOI: `10.1016/0020-7381(75)87021-5`.

[82] *What is an Interferometer?* Available online: `https://www.ligo.caltech.edu/page/what-is-interferometer`.

[83] V. Argueta. *Introduction to interferometers, theory and design types*. Available online: `https://www.opticsforhire.com/blog/interferometers-types-performance-design-considerations`. 2002.

[84] Rachel Berkowitz. "Lab experiments mimic the origin and growth of astrophysical magnetic fields". In: *Physics Today* 71.4 (2018), pp. 20–22. DOI: `10.1063/pt.3.3891`.

[85] Chris Woodford. *Interferometers*. Dostupne z: `Ll`. 2020.

[86] I. V. Lisitsyn et al. "Effect of laser beam deflection on the accuracy of interferometer measurements". In: *Review of Scientific Instruments* 69.4 (1998), pp. 1584–1586. DOI: `10.1063/1.1148868`.

[87] A. Bone. "Shadowgraphy based diagnostics for laser plasma interactions". PhD thesis. Tecnico Lisboa, 2015.

[88] H. Bohlin. *Investigation of the influence of a magnetic field on the formation and evolution of supersonic jets and shocks*. Proposal. 2021.

[89] Wikimedia Commons. *Electromagnetic waves*. Available online: `https://commons.wikimedia.org/wiki/FileElectromagneticwaves.png`.

[90] *Introduction to polarization*. Available online: `Https://www.edmundoptics.com/knowledge-center/application-notes/optics/introduction-to-polarization/`.

[91] K. Zetie. "How does a Mach-Zender interferometer work?" In: *Phys. Edu.* (2000).

[92] *What are Beamsplitters?* Available online: https://www.edmundoptics.com/knowledge-center/application-notes/optics/what-are-beamsplitters/.

[93] M. Takeda. "Fourier transform method of fringe pattern analysis for computer based topography and interferometry". In: *Optical Society of America* (1981).

[94] J. Mazac. *Zapisky z RMF*. Available online: https://wikiskripta.fjfi.cvut.cz/wiki/index.php?title=01RMF&action=latexdoc&ext=pdf. 2022.

[95] J. Sisma. "Vyvoj interferometrickeho systemu VISAR". MA thesis. Czech Technical University, 2018.